Metallicity, temperature, and gravity scales of M subdwarfs

N. Lodieu, F. Allard, C. Rodrigo, Y. Pavlenko, A. Burgasser, Y. Lyubchik, B. Kaminsky, D. Homeier

Metallicity, temperature, and gravity scales of M subdwarfs[*,**]

N. Lodieu[1,2], F. Allard[3,4], C. Rodrigo[5,6], Y. Pavlenko[7,8,4], A. Burgasser[9], Y. Lyubchik[7],
B. Kaminsky[7], and D. Homeier[4,10]

1 Instituto de Astrofísica de Canarias (IAC), Calle Vía Láctea s/n, 38200 La Laguna, Tenerife, Spain
   e-mail: nlodieu@iac.es
2 Departamento de Astrofísica, Universidad de La Laguna (ULL), 38205 La Laguna, Tenerife, Spain
3 Univ. Lyon, ENS de Lyon, Univ. Lyon1, CNRS, Centre de Recherche Astrophysique de Lyon UMR5574, 69007 Lyon, France
4 Visiting Professor at the Instituto de Astrofísica de Canarias (IAC), La Laguna, Tenerife, Spain
5 Departmento de Astrofísica, Centro de Astrobiología (CSIC-INTA), ESAC Campus, Camino Bajo del Castillo s/n,
   286922 Villanueva de la Cañada, Spain
6 Spanish Virtual Observatory, 28692 Villanueva de la Cañada, Spain
7 Main Astronomical Observatory of the National Academy of Sciences of Ukraine, Ukraine
8 Center for Astrophysics Research, University of Hertfordshire, College Lane, Hatfield, Hertfordshire AL10 9AB, UK
9 Center for Astrophysics and Space Science, University of California San Diego, La Jolla, CA 92093, USA
10 Georg-August-Universität Goettingen Institut für Astrophysik, Friedrich-Hund-Platz 1, 37077 Göttingen, Germany

Received 18 February 2019 / Accepted 1 July 2019

ABSTRACT

Aims. The aim of the project is to define metallicity/gravity/temperature scales for different spectral types of metal-poor M dwarfs.
Methods. We obtained intermediate-resolution ultraviolet ($R \sim 3300$), optical ($R \sim 5400$), and near-infrared ($R \sim 3900$) spectra of 43 M subdwarfs (sdM), extreme subdwarfs (esdM), and ultra-subdwarfs (usdM) with the X-shooter spectrograph on the European Southern Observatory Very Large Telescope. We compared our atlas of spectra to the latest BT-Settl synthetic spectral energy distribution over a wide range of metallicities, gravities, and effective temperatures to infer the physical properties for the whole M dwarf sequence (M0–M9.5) at sub-solar metallicities and constrain the latest atmospheric models.
Results. The BT-Settl models accurately reproduce the observed spectra across the 450–2500 nm wavelength range except for a few regions. We find that the best fits are obtained for gravities of $\log(g) = 5.0$–5.5 for the three metal classes. We infer metallicities of [Fe/H] = -0.5, -1.5, and -2.0 ± 0.5 dex and effective temperatures of 3700–2600 K, 3800–2900 K, and 3700–2900 K for subdwarfs, extreme subdwarfs, and ultra-subdwarfs, respectively. Metal-poor M dwarfs tend to be warmer by about 200 ± 100 K and exhibit higher gravity than their solar-metallicity counterparts. We derive abundances of several elements (Fe, Na, K, Ca, Ti) for our sample but cannot describe their atmospheres with a single metallicity parameter. Our metallicity scale expands the current scales available for mildly metal-poor planet-host low-mass stars. Our compendium of moderate-resolution spectra covering the 0.45–2.5 micron range represents an important resource for large-scale surveys and space missions to come.

Key words. subdwarfs – stars: low-mass – techniques: spectroscopic – infrared: stars

1. Introduction

Mass, gravity, temperature, and metallicity constitute key parameters to understand the formation and evolution of all type of stars. M dwarfs represent the largest population of stars among members of the solar neighbourhood (Henry et al. 2006; Bochanski et al. 2010; Kirkpatrick et al. 2012) and have also become attractive targets to search for Earth-like planets (e.g. Nutzman & Charbonneau 2008; Quirrenbach et al. 2012; Sozzetti et al. 2014). While the metal content of solar-type stars can be measured with high accuracy (e.g. Adibekyan et al. 2012), the metallicity of M dwarfs is more difficult to ascertain due to the significant number of absorption bands (Kirkpatrick et al. 1999). Several groups have conducted complementary surveys to assess the metallicity of M dwarfs based on photometry and colours

(Bonfils et al. 2005; Johnson & Apps 2009; Schlaufman & Laughlin 2010; Neves et al. 2012; Hejazi et al. 2015; Dittmann et al. 2016) or high-resolution spectra and spectral synthesis of multiple systems composed of a solar-type primary and an M dwarf secondary at optical and infrared wavelengths (Woolf & Wallerstein 2005, 2006; Bean et al. 2006; Woolf et al. 2009; Rojas-Ayala et al. 2010, 2012; Muirhead et al. 2012; Terrien et al. 2012; Önehag et al. 2012; Neves et al. 2013, 2014; Hejazi et al. 2015; Newton et al. 2015; Lindgren et al. 2016). These surveys usually focus on slightly metal-poor M dwarfs, with metallicities above -1.0 dex. An extension to lower metallicities is needed to complement the precise distances that the *Gaia* satellite (de Bruijne 2012) will provide for a great number of spectroscopically confirmed thick-disk and halo M dwarfs (Savcheva et al. 2014) and also to understand the role of metallicity on the molecules and dust grains present in the atmosphere of low-mass stars.

M subdwarfs (sdMs) are population II dwarfs that appear bluer than solar-metallicity stars due to the dearth of metals in their atmospheres (Baraffe et al. 1997). These stars exhibit thick-disk or halo kinematics, including high proper motions or large heliocentric velocities (Gizis 1997). They belong to the first

---

generation of stars and are important tracers of the chemical enrichment history of the Galaxy. The original classification for sdMs and extreme sdMs (esdMs) developed by Gizis (1997) has been revised and extended by Lépine et al. (2007). A new class of subdwarfs has been added, the ultra-subdwarfs (usdMs). The new scheme is based on a parameter, $\zeta_{\mathrm{TiO/CaH}}$, which quantifies the weakening of the strength of the TiO band (in the optical) as a function of metallicity. Subdwarfs are easily distinguished from dwarfs with solar abundances because they exhibit stronger metal-hydride absorption bands (FeH, CrH) and metal lines (CaI, FeI) as well as blue infrared colours caused by collision-induced H_2–H_2 absorption (Gizis 1997; Lépine et al. 2007; Lodieu et al. 2017). An independent classification scheme based on metallicity, gravity, and temperature has been proposed for M dwarfs by Jao et al. (2008) and an extension to the L dwarf regime proposed by Kirkpatrick et al. (2014) and Zhang et al. (2017).

In this paper, we present moderate-resolution 0.45–2.5 μm spectroscopy of 15 sdMs, 16 esdMs, and 12 usdMs to infer their metallicities and T_{eff} by direct comparison with the latest BT-Settl synthetic models (Allard et al. 2012). In Sect. 2 we present our sample of metal-poor M dwarfs drawn from the literature. In Sect. 3 we describe our spectroscopic observations. In Sect. 4 we introduce the BT-Settl models used to infer the physical parameters of metal-poor M dwarfs. In Sect. 5 we infer the spectral type-versus-metallicity/gravity/T_{eff} relation of the three M dwarf metal classes and compare it to independent but complementary studies as well as solar-type M dwarfs. In Sect. 6 we discuss our results and the peculiarities of some of the spectra.

2. Sample selection

To select our sample of subdwarfs, we used the SDSS spectroscopic database which contains a wealth of high-quality spectra covering the 5000–9200 Å range at a spectral resolution of ~2000. Hundreds of objects have been classified as sdMs, esdMs, or usdMs following the scheme developed by Lépine et al. (2007). This classification is publicly available through the SDSS archive and we have taken advantage of it to retrieve a large sample of low-metallicity M dwarfs.

We selected a sub-sample of low-metallicity stars which represent a sequence going from M0 to M9.5 from optical spectra. The objects were specifically chosen to be the (or among the) brightest of their subclass and be observable either in August or January from the southern hemisphere to achieve the best signal-to-noise ratio possible over a wide wavelength range. We completed our sample with LHS 377 (sdM7; Gizis 1997), observed with the same telescope/instrument but at higher spectral resolution (Rajpurohit et al. 2016). Our final sample contains 15 sdM0–sdM9.5, 16 esdM0.0–esdM8.5, and 12 usdM0.0–usdM8.5) with almost one object per spectral sub-type. We are missing the sdM7.5, sdM8, and sdM9 in the sdM, the esdM2.5 and esdM8 in the esdM sequence, and more usdMs (usdM1.5, usdM2, usdM3.0, usdM6.5, usdM7, and usdM8). We note that these targets were included in our original sample but were not observed during the ESO service runs. Table 1 lists their coordinates, optical SDSSi magnitudes, optical spectral types on the Lépine et al. (2007) scheme, dates of observations, mean airmass, exposure times in all three arms, and numbers of AB cycles for all 43 subdwarfs.

3. VLT/X-shooter spectroscopy

We carried out spectroscopy from the UV- to the K band with the X-shooter spectrograph (D'Odorico et al. 2006; Vernet et al.

2011) mounted on the Cassegrain focus of the Very Large Telescope (VLT) Unit 2. Observations were conducted in service mode by the European Southern Observatory (ESO) staff over the course of three semesters, between August 2012 and June 2014 (Table 1). The conditions at the time of the observations met the clear sky request, with an airmass less than 1.6, grey conditions, and a seeing better than 1.2 arcsec. We set the individual on-source integration times according to the magnitudes of the targets and used the multiple AB patterns to correct for the sky contribution (mainly) in the near-infrared (NIR). All observations were done with the slit oriented at parallactic angle. We list all the M subdwarfs observed with X-shooter in Table 1 along with a summary of the logs of the observations.

X-shooter is a multi wavelength cross-dispersed echelle spectrograph made of three arms covering the ultraviolet (UVB; 0.3–0.55 μm), visible (VIS; 0.55–1.0 μm), and NIR (1.0–2.48 μm) wavelength ranges simultaneously thanks to the presence of two dichroics splitting the light. The spectrograph is equipped with three detectors: a 4096×2048 E2V CCD44-82, a 4096×2048 MIT/LL CCID 20, and a 2096×2096 Hawaii 2RG for the UVB, VIS, and NIR arms, respectively. We set the read-out mode to 400k and low gain without binning. We used the 1.6 arcsec slit in the UVB, 1.5 arcsec in the VIS, and 1.2 arcsec NIR, yielding resolving powers of 3300 (9.9 pixels per full-width-half-maximum), 5400 (9.7 pixels per full-width-half-maximum), and 3900 (5.8 pixels per full-width-half-maximum) in the UVB, VIS, and NIR arms, respectively.

We ran the latest version of the X-shooter pipeline (2.8.0)[1] on the raw data downloaded from the ESO archive with their associated raw calibration files from our three programmes: 089.C-0140(A), 091.C-0264(A), and 093.C-0610(A). All spectra have their instrumental signature removed, including bias and flat-field. The spectra are wavelength-calibrated, sky-subtracted and finally flux-calibrated. The output products include a 2D spectrum associated with a 1D spectrum. However, the optimal extraction of the 1D spectrum not being yet implemented in the version 2.8.0 of the pipeline, we extracted the UVB, VIS, and NIR spectra with the apsum task under IRAF (Tody 1986, 1993). We note that most of the targets have little flux in the UVB arm, resulting in low signal-to-noise ratio below 550 nm and very little flux (or no flux) below 400 nm. We corrected the VIS and NIR spectra for telluric bands/lines with the molecfit package distributed by ESO (Kausch et al. 2015; Smette et al. 2015)[2] mainly because the telluric standards were not necessarily taken at the same airmass as our targets. The regions corrected are: 625–632, 686–696, 716–732, 758–770, 812–834, 893–920, 928–980 nm in the VIS arm and 1105–1220, 1253–1280, 1310–1510, 1730–1995, 2000–2035, 2045–2085, 2200–2470 nm in the NIR arm.

The final spectral energy distributions (SEDs) of sdMs, esdMs, and usdMs are displayed in figures in Appendix A. For display purposes, we shifted the observed spectra to the BT-Settl models because of the large velocities of our subdwarfs taking into account that the wavelength scale of models is in vacuum and the observed spectra in the air system (see Sect. 5). Our sample increases the sample of subdwarfs presented in Rajpurohit et al. (2016) by a factor of five and extends that recent work to the full sequence of the three metallicity classes of M subdwarfs. We will make all spectra publicly available through the late-type subdwarf archive[3] (Lodieu et al. 2017).

---

[1] http://www.eso.org/sci/software/pipelines/
[2] http://www.eso.org/sci/software/pipelines/skytools/molecfit
[3] http://svo2.cab.inta-csic.es/vocats/ltsa/

Table 1. Logs of the VLT/X-shooter spectroscopic observations of M subdwarfs.

RA (J2000)	Dec (J2000)	i'	SpT	Date	Airm	ExpT	Cycles
hh:mm:ss.ss	dd:mm:ss.s	mag				s/s/s	
23:46:59.87	−00:59:43.9	15.166	sdM0.0	13 Aug. 2012	1.30	90/66/66	2AB
21:22:02.76	+00:44:56.8	14.996	sdM0.5	21 May 2012	1.13	90/66/66	2AB
00:48:00.05	+00:28:49.4	15.260	sdM1.0	13 Aug. 2012	1.22	90/66/66	2AB
00:51:25.68	−00:37:16.9	16.666	sdM1.5	18 Aug. 2012	1.10	216/216/240	2AB
23:57:32.54	−01:10:36.3	15.692	sdM2.0	17 Aug. 2012	1.32	90/66/66	2AB
01:17:46.53	−00:01:05.3	16.196	sdM2.5	13 Aug. 2012	1.36	90/66/66	2AB
03:24:49.81	−00:15:05.0	14.942	sdM3.0	15 Aug. 2012	1.14	90/66/66	2AB
02:12:08.59	+00:37:01.5	14.918	sdM3.5	19 Aug. 2012	1.11	90/66/66	2AB
03:46:01.58	+00:55:11.6	15.872	sdM4.0	19 Aug. 2012	1.14	90/66/66	2AB
22:57:48.05	+14:29:39.9	18.336	sdM4.5	07 Jul. 2013	1.39	276/292/300	5AB
00:48:36.45	+00:09:31.7	17.175	sdM5.0	10 Jan. 2012	1.32	90/66/66	AB
23:53:36.94	+00:47:34.1	18.025	sdM5.5	14 Jul. 2013	1.26	276/292/300	5AB
00:25:52.59	+01:09:24.9	17.797	sdM6.0	19 Aug. 2012	1.18	266/266/290	5AB
16:10:28.99	−00:40:53.0	15.903	sdM6.5	10 Jun. 2012	1.11	90/66/66	2AB
02:05:33.75	+12:38:24.0	18.107	sdM8.0	11 Aug. 2012	1.30	266/266/290	5AB
10:13:07.35	−13:56:20.4	16.010	sdM9.5	09 May 2013	1.34	126/142/150	1AB
01:37:55.30	−09:39:41.9	17.488	esdM0.0	08 Sep. 2013	1.45	276/292/300	5AB
23:25:41.30	+00:04:19.6	16.203	esdM0.5	18 Aug. 2012	1.13	90/66/66	2AB
00:38:02.86	+00:50:14.2	17.520	esdM1.0	14 Jul. 2013	1.20	276/292/300	5AB
23:40:39.45	−00:51:18.4	16.263	esdM1.5	12 Aug. 2012	1.49	90/66/66	2AB
12:55:29.19	−03:30:55.8	17.536	esdM2.0	11 Jul. 2013	1.18	276/292/300	5AB
12:53:53.35	+12:12:48.7	16.531	esdM3.0	11 Jul. 2013	1.30	126/142/150	3AB
14:52:04.63	+10:18:26.3	17.892	esdM3.5	30 Jun. 2014	1.22	276/292/300	5AB
00:40:18.18	−10:41:55.9	17.405	esdM4.0	18 Aug. 2012	1.04	276/292/300	5AB
01:09:54.11	−10:12:12.6	14.766	esdM4.5	04 Aug. 2013	1.05	126/142/150	1AB
13:31:51.15	−00:09:19.0	18.180	esdM5.0	15 Jun. 2013	1.16	276/292/300	5AB
09:03:07.95	+08:42:43.2	15.988	esdM5.5	18 Apr. 2014	1.20	126/142/150	1AB
15:36:47.08	+02:55:01.5	19.071	esdM6.0	12 Aug. 2012	1.14	276/276/300	6AB
01:33:46.24	+13:28:22.4	17.830	esdM6.5	04 Aug. 2013	1.37	276/292/300	5AB
02:35:57.61	+01:08:00.5	19.190	esdM7.0	09 Sep. 2013	1.11	456/472/480	4AB
05:58:58.91	−29:03:26.7	16.320	esdM7.5	27 Aug. 2012	1.34	216/216/240	2AB
04:52:09.94	−22:45:08.4	17.220	esdM8.5	17 Aug. 2012	1.13	216/216/240	2AB
03:27:28.10	−00:50:01.4	17.462	usdM0.0	16 Sep. 2012	1.09	266/266/290	5AB
15:34:04.63	+09:36:22.5	17.984	usdM0.5	09 Aug. 2013	1.22	266/266/290	5AB
15:12:18.36	+09:30:40.7	17.890	usdM1.0	23 Jul. 2013	1.23	276/292/300	5AB
20:59:20.57	+00:00:33.4	17.853	usdM2.5	11 Aug. 2012	1.12	266/266/290	5AB
10:41:07.20	+06:33:04.7	18.062	usdM3.0	31 May 2013	1.27	246/262/270	5AB
15:35:40.74	+08:21:43.3	18.008	usdM4.0	10 Aug. 2013	1.21	276/292/300	5AB
14:17:48.62	+07:11:05.4	17.658	usdM4.5	12 Jul. 2013	1.18	276/292/300	5AB
12:04:26.91	+13:29:23.3	16.549	usdM5.0	12 Jun. 2012	1.33	216/216/240	2AB
16:27:54.22	+00:37:14.0	18.384	usdM5.5	17 Aug. 2012	1.15	266/266/290	5AB
16:41:23.73	+24:49:42.4	17.233	usdM6.0	15 Jul. 2013	1.58	126/142/150	3AB
08:22:33.69	+17:00:19.9	17.300	usdM7.5	03 Apr. 2013	1.39	126/142/150	3AB
12:27:05.06	−04:47:20.7	16.630	usdM8.5	11 Jul. 2013	1.35	126/142/150	3AB

Notes. We list the coordinates and Sloan i' magnitude, the spectral type from the SDSS spectroscopic database, the date of the VLT X-shooter with the airmass at the beginning of the observations, the on-source integrations in each arm (UVB/VIS/NIR) with the numbers of AB cycles (identical for all arms).

4. BT-Settl synthetic spectra

To infer the range of physical parameters (gravities i.e. $\log(g)$, metallicities [M/H], and $T_{\rm eff}$) for our sequence of subdwarfs, we employed the BT-Settl models (Allard et al. 2003, 2007; Allard & Freytag 2010; Allard et al. 2012) available for retrieval at the webpage[4] of France Allard. The BT-Settl models account for TiO (Plez 1998, 2008) and H_2O (Barber et al. 2006) among

other opacities using the Caffau et al. (2011) abundance values and mixing information for the CO^5BOLD code (Steiner et al. 2007; Freytag et al. 2010). These models are valid for a wide range of $T_{\rm eff}$ (400–8000 K), gravities ($\log(g) = 2.5$–6.0 dex), and metallicities (from −5.0 to solar). The synthetic SEDs span the wavelength range from 10 Å up to 1000 μm. The stellar metallicity is defined by the total iron content of a star because iron is the easiest species to measure spectroscopically. The abundance ratio [Fe/H] is defined as the logarithm of the ratio of the iron abundance of a star compared to that of the Sun, where −1.0 dex

---

4 http://perso.ens-lyon.fr/france.allard/

means that a star has one tenth of the solar metallicity. The determination of the metallicity is only valid if the abundances of all elements follow the abundance of iron. However, this statement might not be entirely true in the case of halo dwarfs that have suffered different nucleosynthesis events.

We downloaded the spectra from the CIFIST2011 grid[5] and considered the ranges that encompass the spectral types of the three metallicity classes: $T_{\rm eff} = 4000$–2500 K, gravity (log $g = 4.5$–5.5 dex), and metallicity [M/H] (from -2.5 dex to solar). These models assume solar abundance values ($Z = 0.0153$, $Z/X = 0.0209$) from Caffau et al. (2011) with alpha enhancement taken into account as follows: [alpha/H] $= +0.2$ relative to solar for [M/H] $= -0.5$ dex and [alpha/H] $= +0.4$ for lower metallicities. For direct comparison, we limited the wavelength range to 450–2500 nm and smoothed the synthetic SEDs with the Interactive Data Language (IDL) `gaussfold` function[6] to the spectral resolution of our X-shooter spectra.

Throughout the paper, we use the term metallicity [Fe/H] which is given by the BT-Settl models. We do not infer abundances or metallicities of single elements but the global values given by the synthetic spectra. The former can differ from the latter as shown for a metal-poor low-mass binary (Pavlenko et al. 2015). The study of abundances of individual elements in subdwarfs is beyond the scope of this paper but will be investigated in a future publication.

5. Comparison: observations vs. models

We fitted the observed spectra with the BT-Settl SEDs with a chi-square (χ^2) minimisation procedure described in Sect. 5.1. We derived the temperature (Sect. 5.2) and metallicity (Sect. 5.4) scales from the best model fits.

5.1. Chi-square fitting

We performed a χ^2 fit to compare the observed spectra with those in the BT-Settl theoretical library. We considered the following ranges in temperature, gravity, and metallicity: 4000–2500 K, log $g = 4.5$–6.0 dex, and [M/H] between -3.0 and 0.0 dex, as expected for old low-mass M-type dwarfs. The steps are 100 K and 0.5 dex in temperatures and gravity + metallicity, respectively. We ignored regions of the observed spectra strongly affected by telluric bands, in particular the 530–570 nm, 928–1010 nm, 1110–1150 nm, 1340–1460 nm, and 1790–1970 nm wavelength ranges.

We shifted our observed spectra to the wavelength of the models. We calculated the heliocentric radial velocities for our sample of metal-poor M dwarfs using a set of about 15 lines (potassium, sodium, iron, and calcium) in the 610–840 nm wavelength range, the exact number depending on the quality of the spectrum and strength of the line (Table 2). We measured consistent shifts between these five strong lines for all sources, with dispersions of the order of a few kilometres per second. We assume that the true error bars are set by the resolution of our X-shooter spectra (3900–6700), corresponding to radial velocity uncertainties of approximately 15–25 km s^{-1}.

We then minimized the χ^2 value for each observed and theoretical spectrum, as:

$$\chi^2 = \frac{1}{N} \sum_i \left\{ \frac{(F_{\rm obs,i} - A\, F_{\rm mod,i})^2}{(\Delta F_{\rm obs,i})^2} \right\}. \tag{1}$$

The scale factor A is calculated to minimize χ^2 for each case as:

$$A = \frac{\sum_i (F_{\rm obs,i} F_{\rm mod,i}/\Delta F_{\rm obs,i}^2)}{\sum_i (F_{\rm mod,i}^2/\Delta F_{\rm obs,i}^2)}. \tag{2}$$

In both expressions the sum is performed over the full wavelength range. The factors $F_{\rm obs,i}$ and $\Delta F_{\rm obs,i}$ are the observed values of the flux and its associated errors, respectively, and $F_{\rm mod,i}$ are the corresponding values of the theoretical spectrum.

To prevent points with small observational errors from having an excessive weight in the fitting process, we calculated the average of the error values in each spectrum as:

$$|\Delta F_{\rm obs}| = \frac{1}{N} \sum_i \Delta F_{\rm obs,i}. \tag{3}$$

We then fixed the error to be half the average for those points with smaller errors during the fitting process.

Overall, we find that BT-Settl models accurately reproduce the SEDs of metal-poor M dwarfs and in particular the main molecular bands. However, we noticed that some of the main atomic lines are not well reproduced: (Figs. A.13–A.15). The lines of the sodium doublet at ~820 nm predicted by the BT-Settl models appear too broad for spectral types later than approx M5. The calcium lines seem too narrow for usdMs but look correctly reproduced for sdMs and esdMs. This mis-match between observations and models leads to over- or underestimations of the abundances of these elements. The disappearance of these elements in other molecules (e.g. CaOH) could also explain the observed discrepancy. We note that the potassium doublet at around 760/790 nm is well reproduced by the models, except for the latest spectral types (≥M7) and the coolest sources (Figs. A.13–A.15).

As a consequence, we opted for four fitting procedures to gauge the uncertainties on the physical parameters derived from the synthetic spectra.

1. "FF" corresponds to the fit of the full SED of each subtype and metal class from 450 to 2500 nm (Figs. A.1–A.3).
2. "LL" corresponds to the fitting procedure of a few lines in the optical spectra (KI and NaI). The model spectra shown correspond to the physical parameters derived from the line fits (Figs. A.4–A.6).
3. "FL": corresponds to a fitting procedure where we fix the temperature derived from the full fit and adjust gravity and metallicity to converge towards the best fit of the aforementioned lines (Figs. A.7–A.9).
4. "LF": corresponds to a fitting procedure where we fix the gravity and metallicity from the fits of the line and adjust the effective temperature fitting the full SED of each subtype and subclass. (Figs. A.10–A.12).

In general, we find that the "FF" fitting procedure reproduces the best all observed spectra. Therefore, we conclude that the physical parameters derived from this option are the most probable.

We list the model-dependent physical parameters in Table 2 and display the best fits provided by the synthetic SEDs (red lines) to observed X-shooter spectra (black lines) for each metal class in Appendix A.

We also looked at the physical parameters derived from the model fit to the optical region of the X-shooter spectra

Table 2. Adopted physical parameters for sdMs, esdMs, and usdMs from the comparison between the observed VLT/X-shooter spectra and the BT-Settl synthetic spectra from the fit of the overall SED.

SpT	sdM					esdM					usdM				
	RV	log g	T_{eff}	[Fe/H]	Mass	RV	log g	T_{eff}	[Fe/H]	Mass	RV	log g	T_{eff}	[Fe/H]	Mass
	km s^{-1}	dex	K	dex	$M_\odot$	km s^{-1}	dex	K	dex	$M_\odot$	km s^{-1}	dex	K	dex	$M_\odot$
M0.0	+122.6	4.5	3600	−1.5	0.133	−9.2	5.0	3800	−1.0	0.275	+122.6	4.5	3500	−2.0	0.106
M0.5	−45.1	5.0	3700	−1.0	0.216	−97.3	5.0	3700	−1.5	0.153	−117.1	5.5	3700	−2.5	0.125
M1.0	−33.7	5.0	3700	−0.5	0.352	−259.7	5.5	3800	−0.5	0.421	−15.9	5.5	3700	−1.0	0.216
M1.5	−78.7	4.5	3600	−0.0	0.600	−46.7	5.0	3600	−1.0	0.178	–	–	–	–	–
M2.0	−133.8	5.5	3600	−0.5	0.272	+40.6	5.5	3600	−1.0	0.178	–	–	–	–	–
M2.5	−39.7	5.5	3600	−0.5	0.272	–	–	–	–	–	−138.8	5.5	3600	−1.5	0.133
M3.0	−52.6	5.0	3500	−0.0	0.450	+35.3	5.5	3500	−1.5	0.120	+178.0	6.0	3800	−0.5	0.421
M3.5	−21.7	5.0	3400	−0.5	0.177	−52.5	5.5	3500	−1.5	0.120	–	–	–	–	–
M4.0	−67.2	5.0	3400	−1.0	0.129	−81.3	5.5	3400	−1.5	0.110	−19.8	4.5	3200	−1.5	0.098
M4.5	−470.7	5.5	3300	−1.0	0.117	−60.7	5.5	3400	−1.0	0.129	−102.5	5.5	3400	−2.0	0.100
M5.0	−31.6	5.0	3200	−0.0	0.150	+21.7	4.5	3200	−1.5	0.098	+180.0	5.5	3500	−2.5	0.106
M5.5	−12.5	5.5	3200	−1.0	0.107	+318.1	5.5	3300	−2.0	0.098	−25.1	4.5	3300	−2.0	0.098
M6.0	−87.8	5.5	3200	−1.0	0.107	−38.5	5.5	3300	−2.0	0.098	+104.8	5.5	3300	−2.0	0.098
M6.5	−57.2	5.5	2900	−0.0	0.063	−3.7	5.5	3300	−2.0	0.098	–	–	–	–	–
M7.0	–	5.0	3000	−1.0 $^{(a)}$	0.096	−167.1	5.5	3200	−0.0	0.096	–	–	–	–	–
M7.5	–	–	–	–	–	+191.1	5.0	3000	−2.0	0.090	+122.1	5.5	3100	−2.5	0.092
M8.0	−208.9	5.5	2900	−2.0	0.089	–	–	–	–	–	–	–	–	–	–
M8.5	–	–	–	–	–	+72.7	5.5	3000	−2.0	0.090	+85.0	5.5	3100	−2.5	0.092
M9.5	+64.7	5.0	2800	−2.0	0.088	–	–	–	–	–	–	–	–	–	–

Notes. For each spectral subtype and metal class, we list the radial velocities (RV in km s^{-1}), gravity (log g), temperature (T_{eff} in K), and metallicity ([Fe/H]). Uncertainties on the radial velocities, gravities, T_{eff}, and metallicities are 15–25 km s^{-1}, 0.5 dex, 100 K, and 0.25 dex, respectively. Uncertainty on mass from the Baraffe et al. (1997) models is approximately ±10%. No X-shooter spectrum is available for the subtype with missing values. $^{(a)}$LHS 377 parameters are from Rajpurohit et al. (2016).

(600–1000 nm) from which the spectral classification of subdwarfs is based (Gizis 1997; Lépine et al. 2007). We find that on average the optical spectra give equal or cooler effective temperatures, lower gravities, and/or lower metallicities (Table B.5).

5.2. Temperature scale

We derived comparable T_{eff} intervals for all three metallicity classes (Table 2) fitting the full SEDs (Tables B.1 and B.3). The T_{eff} range from ∼3800 K for the earlier sdMs down to ∼2600 K for the latest spectral types. We can hardly distinguish the three classes in the diagram showing T_{eff} versus spectral type in Fig. 1 within the error bars of 100 K set by the steps available in the models. We overplotted the temperature scale of field M dwarfs (solid black line in Fig. 1) from the latest relation of Rajpurohit et al. (2013), the trend of which is comparable to earlier studies within error bars (Bessell 1991; Leggett et al. 1996, 2000; Testi 2009). Dwarfs with spectral types earlier than M2 are indistinguishable in the temperature parameter space. Overall, the temperatures of metal-poor M dwarfs are similar to those of solar-type M dwarfs with an offset of 200 ± 100 K towards warmer temperatures. They follow a linear trend with some spectral types being off by 100 K or 200 K, which may be due to the error on the spectral classification or binarity which is mainly based on a spectral index measuring the strength of the CaH and TiO bands in the optical (Lépine et al. 2007).

We note that the temperature scale of the line fitting option tends to infer lower effective temperatures by at least 100 K with a similar interval for temperatures hotter than 3400 K, producing ranges of 3700–2700 K. The agreement is better at lower

temperatures and within the uncertainty of 100 K (Tables B.2 and B.4). We also find that the fit to the optical region only yields typically lower effective temperature by 100 K–200 K (Table B.5).

5.3. Gravity scale

Subdwarfs are old low-mass stars that belong to the thick disk or halo of our Galaxy. On average, they are much older than their solar-metallicity counterparts. Monteiro et al. (2006) identified several white dwarf–subdwarf systems in the thick disk and derived ages of 6–9 Gyr for two of them with M subdwarf companions. From the comparison with FGK stellar templates selected as benchmarks for the *Gaia* mission (Jofré et al. 2014), Scholz et al. (2015) inferred a possible age of 12 Gyr for an ancient metal-poor (−2.0 ± 0.2 dex) F-type star member of the Galactic halo due to its large tangential velocity. On average, we expect our sample to be older than 5 Gyr.

From the fit of the BT-Settl models to the full VIS+NIR SED of our M subdwarfs, we infer gravities of 4.5–5.5 dex for all metal classes, except for one object with log (g) = 6.0 dex (usdM3.0; see discussion section). However, we observe a possible trend of increasing mean gravity with lower metallicity, going from 5.0 dex for sdMs to 5.5 dex for esdMs and usdMs (Fig. 2). We note that the range of gravities of the CIFIST models is limited to 6.0 dex but higher gravities are desirable to corroborate this statement. We also note that the fit to the optical region only yields typically lower gravities by 0.5–1.0 dex (Table B.5).

If we average the gravities for the metallicities derived from the model fit independently from the metal class (i.e. sdMs, esdMs, usdMs), we observe that targets with metallicities of
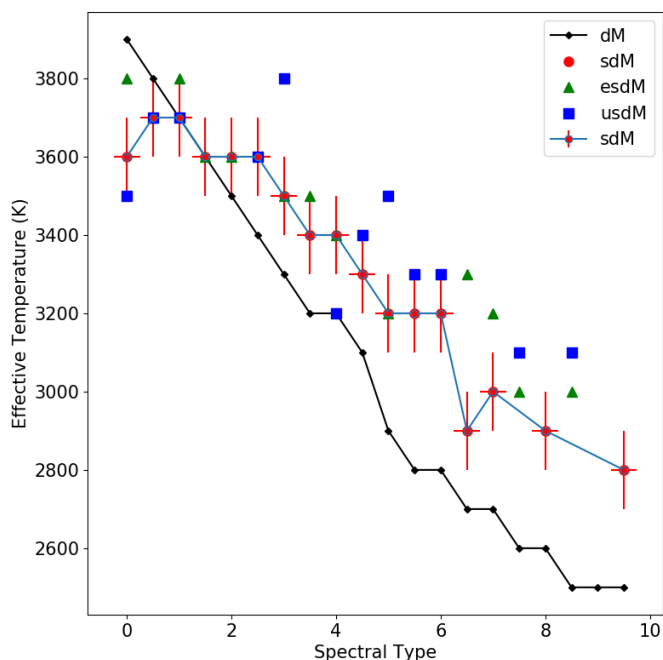
Fig. 1. T_{eff} as a function of spectral type for solar-metallicity M dwarfs (black diamonds with line), sdMs (red dots), esdMs (green triangles), and usdMs (blue squares). Error bars on spectral types and model parameters are marked for sdMs only for clarity purposes. Error bars on spectral type and temperatures are ±0.25 and ±100 K, respectively. The point for the sdM7 subdwarf corresponds to LHS 377 from Rajpurohit et al. (2016).
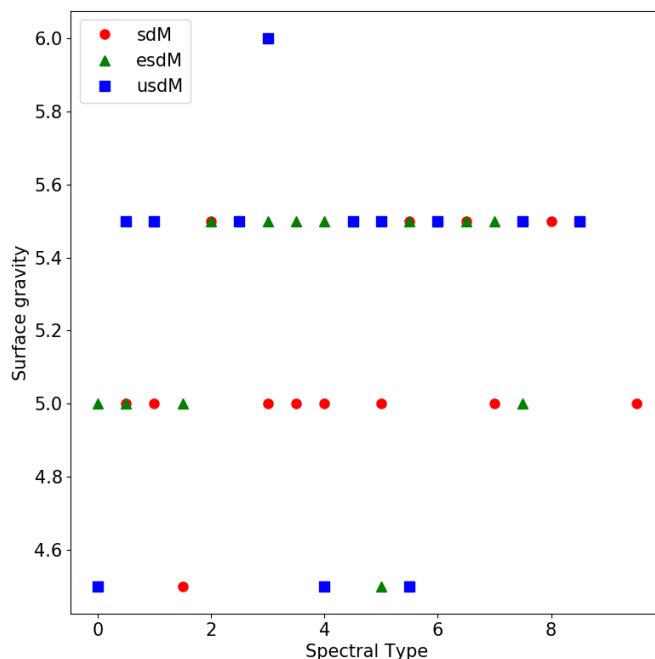

Fig. 2. Gravity as a function of spectral type for sdMs (red dots), esdMs (green triangles) and usdMs (blue squares). Error bars on spectral type and gravity are ±0.5 and ±0.5 dex, respectively. The point for the sdM7 subdwarf corresponds to LHS 377 from Rajpurohit et al. (2016).

−0.5 dex have on average lower gravities (∼4.9 dex) than more metal-poor objects where mean gravities lie between 5.2 and 5.3 dex. The difference in gravity between field M dwarfs and M subdwarfs is below our error bar of 0.5 dex, while the difference between metallicities is five times smaller than our error bars.

5.4. Metallicity scale

Our work extends the current metallicity scale of M dwarfs to metallicities below −0.5 dex with an accuracy on the calibration of the order of 0.25–0.5 dex. The classification is available in the optical for subdwarfs (Gizis 1997; Lépine et al. 2007; Jao et al. 2008; Savcheva et al. 2014; Kesseli et al. 2017) but this is the first time this has been attempted for a large sample of M0–M9 dwarfs (see also Rajpurohit et al. 2016). The determination of the metallicity scale of subdwarfs is key for several reasons. First, the range of metallicities for M subdwarfs is presently poorly constrained for these objects that represent the first generation of stars and are key sources to study the chemical evolution of our Galaxy. On the other hand, M dwarfs are becoming popular to search for low-mass planets by the radial velocity and transit techniques, leading independent groups to look at their metallicity. Nonetheless, all the studies referenced in the introduction focussed on M dwarfs with metallicity slightly below solar with calibrations accurate to <0.15 dex either photometrically (Bonfils et al. 2005; Johnson & Apps 2009; Schlaufman & Laughlin 2010; Neves et al. 2012; Hejazi et al. 2015; Dittmann et al. 2016) or spectroscopically (Woolf & Wallerstein 2005, 2006; Bean et al. 2006; Woolf et al. 2009; Rojas-Ayala et al. 2010, 2012; Muirhead et al. 2012; Terrien et al. 2012; Önehag et al. 2012; Neves et al. 2013, 2014; Hejazi et al. 2015; Newton et al. 2015; Lindgren et al. 2016).

The number of M dwarf hosts below $0.5\,M_\odot$ and with metallicities lower than −0.5 dex is extremely small (≤0.2%) compared to the 3396 confirmed planets[7]. Only three metal-poor M dwarfs have one or several planets: Kapteyn (sdM1.0; Fe/H = −0.86 dex; Anglada-Escudé et al. 2014; Robertson et al. 2015), GJ 667 (K3V+K5V; Fe/H = −0.55 dex; Feroz & Hobson 2014; Anglada-Escudé et al. 2013; Delfosse et al. 2013), and Kepler 1124 (Fe/H = −0.59 dex; Morton et al. 2016). Another four Kepler M stars with masses in the range 0.5–$0.6\,M_\odot$ and metallicities between −0.5 and −1.0 harbour planets.

We present VLT/X-shooter spectra at resolutions of 5400 and 3900 in the VIS and NIR arms, respectively. We estimate metallicities that rely on models and synthetic spectra whose steps are 0.5 dex, which we set as our error bars. Overall, we find that the overall SEDs of sdMs, esdMs, and usdMs are best reproduced by metallicities between solar and −1.0 dex, −1.0 and −2.0 dex, and −1.0 and −2.5 dex, respectively (Fig. 3). We note that a few sdMs have solar metallicities, including the sdM6.5 (1610−0040), a known astrometric binary (Koren et al. 2016) with a mix of spectral features typical of both L subdwarfs and solar-type M dwarfs (Lépine et al. 2003; Reiners & Basri 2006; Cushing & Vacca 2006). We also emphasise that the two coolest sdMs (sdM8 and sdM9.5) in our sample have on average lower metallicities than sdMs earlier than sdM7, suggesting saturation of the metallicity index (Lépine et al. 2007) used in the classification of subdwarf (Zhang et al. 2017). We conclude that there is a trend towards lower mean metallicity from sdMs (−0.5 ± 0.5 dex) to esdMs (−1.5 ± 0.5 dex), and usdMs (−2.0 ± 0.5 dex), consistent with the original definition of these three metal classes. However, we observe variations from one object to another, preventing us from assigning a given M/H for each metal class. We note that the metallicity scale of the line fitting option differs significantly

---

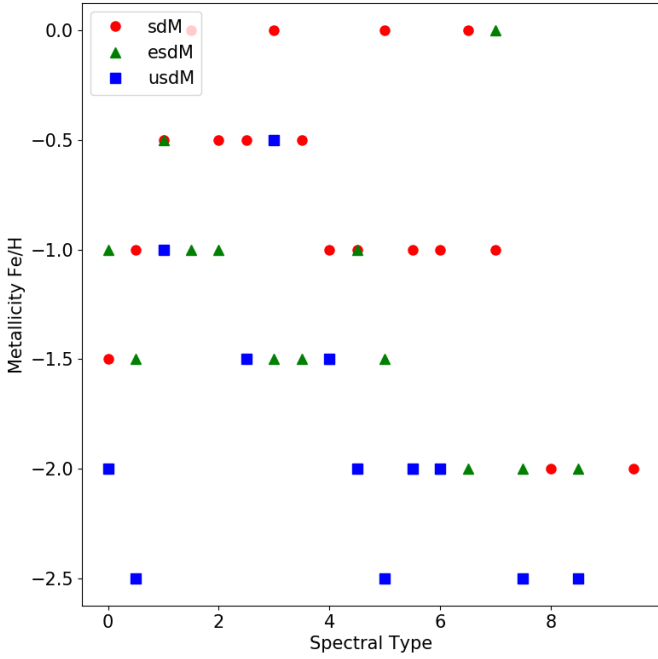[7] Last update on 10 October 2016 at exoplanetarchive.ipac.caltech.edu

Fig. 3. Metallicity as a function of spectral type for sdMs (red dots), esdMs (green triangles) and usdMs (blue squares). Error bars on spectral type and metallicity are ±0.5 and ±0.5 dex, respectively.

from the fit of the SEDs, producing lower metallicities by at least 1.0 dex. (Tables B.2 and B.4). We find the same trend if we consider only the optical range (600–1000 nm) for our fitting procedure.

We compared our global results to the recent analysis of Rajpurohit et al. (2016) also based on VLT/X-shooter spectra but for a much smaller sample of subdwarfs: six sdMs (five sdM0.5–M3 and sdM7), two esdMs (esdM2 and esdM4), and usdM4.5. In their Table 2, they list two possible fits, which usually differ by either 100 K or 0.5 dex in gravity or metallicity. Our physical parameters agree with their results within 1–2σ of the steps of the synthetic SEDs (Table 2). The difference can be explained by the uncertainties on the spectral types, typically 0.5 sub-type. We conclude that both $T_{\rm eff}$-versus-spectral type relations are consistent within current error bars on observational and theoretical sides. Moreover, as stated in Rajpurohit et al. (2016), these results are fully consistent with the physical parameters derived from higher-resolution optical spectroscopy (Rajpurohit et al. 2014).

We can also compare our work to the physical parameters of the metal-poor binary G 224−58 AB composed of a esdK5 and a esdM5.5. Pavlenko et al. (2015) derived the temperature and gravity for the secondary ($T_{\rm eff} = 3200 \pm 100$ K, $\log g = 5.0 \pm 0.5$), and inferred the metallicity from the primary ([Fe/H] = −1.92 dex). Their parameters are in good agreement with our values for the esdM5.5 (SDSS J09030795+0842432) in our sample: $T_{\rm eff} = 3300 \pm 100$ K, $\log g = 5.5 \pm 0.5$ dex, and [Fe/H] = −1.5 ± 0.5 dex (Table 2). Their abundance analysis suggests that many elements (e.g. calcium; [Ca/H] = −1.39 ± 0.03) are over-abundant compared to iron. We do also find that, although the BT-Settl SEDs accurately reproduce the molecular bands of the observed spectra, they fail to fit the atomic lines of many elements like Fe, K, Na, and Ca. In other words, the atomic lines from the BT-Settl models are too broad and over-estimate the abundances of single elements (see Sect. 5.6). The disappearance of these elements in other molecules (e.g. CaOH) could also explain the observed discrepancy.

Table 3. Spectral regions, elements, and their numbers of lines considered to derive abundances of our sample of subdwarfs.

Wavelength range	Elements	# lines
5750–5995 Å	Na, Ti, Ca, Fe	2, 1, 1, 1
7640–7730 Å	K	2
8080–8350 Å	Na, Fe	3, 1
8300–8850 Å	Ca, Ti, Fe	3, 10, 7

5.5. Masses

We inferred model-dependent masses for our sample of subdwarfs from their temperatures looking at the predictions of the NextGen models (Baraffe et al. 1997) and assuming ages of 10 Gyr for these old objects. Although this approach is not correct due to the different inputs physics in the NextGen and BT-Settl grids (computation available on France Allard's webpage; Baraffe et al. 2015), it provides estimates on the masses of these low-metallicity M dwarfs. We derived masses below 0.35 $M_\odot$ for the most massive M subdwarfs down to ~0.087 $M_\odot$ for the coolest objects in our sample, i.e. close to the stellar/substellar boundary with uncertainties of the order of 10% (Table 2). We note that the gravities quoted by the Baraffe et al. (1997) models are in the range $\log (g) = 5.0$–5.5 dex, consistent with the aforementioned gravities derived from the synthetic SEDs within the error bars of 0.5 dex.

5.6. Abundances

We decided to work with the temperatures, gravities, and metallicities derived from the best fits to the optical regions only (Table B.5) to derive the abundances of several elements (Table 3). The relatively low resolution and reduced signal-to-noise ratios of the observed spectra limit the accuracy of our results. Moreover, we work here with metal-deficient stars, in which spectra are not critically affected by blending effects. We carried out the minimization procedure using the PHOENIX model atmospheres to compute synthetical spectra with the WITA program Pavlenko (1997). In these computations, we accounted for the main molecular opacity sources, as described in Pavlenko et al. (2015) and Pavlenko (2014). We employed the atomic line information from the VALD2 and VALD3 databases (Kupka et al. 1999; Ryabchikova et al. 2011). We selected a few spectral ranges with well-defined atomic lines and fitted them in the framework of the LTE approach to determine abundances of several elements listed in Table 3.

To determine the abundances, we compared the residuals of the fluxes and reduced to the local continuum or pseudo-continuum of the observed spectra. We determined these continua/pseudo-continua for all spectral ranges given in Table 3. We carried out the computations for a 20-points abundance grid with a step 0.1 dex around the mean abundance for each metal and spectral subclass. The abundances correspond to over-abundances if they are positive, fixing the iron abundances to the metallicity derived from the model fit of the optical region, assuming a solar abundance of iron of −4.55 dex (Asplund et al. 2009).

When several lines are present in a given spectral range, we average the values of each abundance. We give the uncertainties on the abundances rounded to the nearest integer for a range of ±100 K in effective temperature, which represents the error on our model fits (and the step of the models). We note that the

sodium, potassium, and neutral calcium lines are the most sensitive to small changes in effective temperature due to the low ionisation potentials. We estimate the formal accuracy of the abundance determination to be ±0.1 dex due to several uncertainties in the procedure, such as low signal-to-noise ratio and the determination of the levels of the continuum and pseudo-continuum. We list the final abundances of five elements (Na, K, Ca, Ti, and Fe) with their uncertainties in Table 4. Some of the stars, marked with an asterisk, have spectra with low signal-noise ratios, and therefore the abundances should be interpreted with caution.

We should note that any significant changes in the abundance of alkali metals affect the fluxes of the continuum and hence, the strength of the lines. Alkali metals (Na, K, Ca, Mg) are known donors of free electrons in atmospheres of late-type stars. In our case, we re-computed the continuum fluxes for all the abundances, and so in a first approach we accounted for the effect of opacity changes. However, these changes of abundances may affect the temperature structure of the model atmosphere, changes not accounted for because we employed model atmospheres with a fixed temperature structure.

Our abundance analysis was performed for the model parameters obtained from the fits to observed SEDs (Sect. 4). Furthermore, the resolution of the fitted spectra was not high enough to get high-quality results. On the other hand, we work here with metal-deficient stars, in which spectra are not critically affected by blending effects. We determined a few spectral ranges with well defined atomic lines and fitted them in framework of the LTE approach. Despite all factors constraining the accuracy of our analysis we obtain several relatively robust results:

– We see a shift of Ti abundance distribution towards larger metallicities with respect to Fe for the lowest metallicities (top left panel of Fig. 4).

– We observe a Ca over-abundance in the atmospheres of all subdwarfs (top right panel of Fig. 4). This result agrees with the known enhancement of α elements in the atmospheres of halo dwarfs (e.g. Francois 1986; Nissen et al. 1994; Gratton & Sneden 1994; Fuhrmann et al. 1995).

– We find that K tends to be over-abundant at higher metallicities, that is the opposite effect to Na (middle panels of Fig. 4). This difference increases with lower metallicity and is most notable for usdMs. Perhaps these elements have different chemical histories. The difference is clearly seen in the comparison plot of the distribution of both species where the three metal classes are relatively well separated (bottom panel of Fig. 4).

– We cannot describe the abundances in the atmospheres of our targets with one parameter metallicity (Table 4 and Fig. 4).

6. Discussion

We observe that on average the optical range of the subdwarf spectra yields cooler temperatures, and lower gravities and metallicities. Hence, the availability of the NIR slope is quite important to determine the physical parameters of the three metal classes and break down the temperature-metallicity degeneracy present in the analysis of the sole visible range. The temperature sequence is well determined for all metal classes, with the earliest spectral types being the warmest cases. The metallicity is on average lower for the usdMs, with all three metal class being more metal poor than solar as expected. Those results are however global, with the physical parameters being sensitive to steps of the models in temperature, gravity, and metallicity. Smaller changes in those parameters are most likely limited by the quality (signal-to-noise ratio) and resolution of the X-shooter spectra.

Table 4. Abundances for five elements (sodium, potassium, calcium, titanium, and iron) for each subtype and each metal class for a model atmosphere with a fixed temperature structure.

SpT	Model	Na	K	Ca	Ti	Fe
sdM0.5	3700-4.5-1.0	$0.3^{+0.3}_{-0.2}$	$0.7^{+0.4}_{-0.3}$	$1.2^{+0.0}_{-0.0}$	$0.9^{+0.1}_{-0.1}$	$0.9^{+0.1}_{-0.0}$
sdM1.0	3700-5.0-0.5	$0.2^{+0.2}_{-0.2}$	$0.3^{+0.3}_{-0.3}$	$0.5^{+0.1}_{-0.2}$	$0.4^{+0.1}_{-0.1}$	$0.4^{+0.1}_{-0.1}$
sdM1.5$^{(*)}$	3400-4.5-1.5	$0.4^{+0.1}_{-0.1}$	$0.6^{+0.2}_{-0.2}$	$1.0^{+0.0}_{-0.0}$	$0.5^{+0.1}_{-0.1}$	$0.5^{+0.1}_{-0.1}$
sdM2.0$^{(*)}$	3500-4.5-1.0	$0.7^{+0.2}_{-0.2}$	$1.0^{+0.3}_{-0.3}$	$0.9^{+0.0}_{-0.0}$	$0.5^{+0.1}_{-0.1}$	$0.5^{+0.1}_{-0.1}$
sdM2.5$^{(*)}$	3500-4.5-1.0	$0.6^{+0.2}_{-0.2}$	$0.9^{+0.3}_{-0.3}$	$0.7^{+0.0}_{-0.0}$	$0.6^{+0.1}_{-0.1}$	$0.5^{+0.1}_{-0.1}$
sdM3.0	3500-5.0-0.0	$-0.2^{+0.1}_{-0.1}$	$0.6^{+0.2}_{-0.2}$	$0.2^{+0.0}_{-0.0}$	$0.0^{+0.1}_{-0.1}$	$0.1^{+0.0}_{-0.0}$
sdM3.5	3400-5.0-0.5	$0.2^{+0.2}_{-0.2}$	$0.3^{+0.2}_{-0.3}$	$0.3^{+0.1}_{-0.0}$	$0.3^{+0.2}_{-0.2}$	$0.1^{+0.1}_{-0.1}$
sdM4.0	3400-5.5-0.5	$-0.1^{+0.3}_{-0.2}$	$0.2^{+0.2}_{-0.3}$	$0.8^{+0.0}_{-0.0}$	$0.4^{+0.2}_{-0.1}$	$0.2^{+0.0}_{-0.1}$
sdM4.5	3100-4.5-1.5	$0.5^{+0.2}_{-0.2}$	$0.6^{+0.3}_{-0.3}$	$0.6^{+0.0}_{-0.0}$	$0.9^{+0.0}_{-0.3}$	$0.4^{+0.0}_{-0.1}$
sdM5.0$^{(*)}$	3200-5.5-0.0	$0.5^{+0.2}_{-0.2}$	$0.3^{+0.4}_{-0.2}$	$0.0^{+0.0}_{-0.0}$	$0.3^{+0.3}_{-0.2}$	$0.1^{+0.2}_{-0.2}$
sdM5.5	3200-5.5-1.0	$0.0^{+0.2}_{-0.2}$	$0.1^{+0.3}_{-0.2}$	$0.4^{+0.2}_{-0.2}$	$0.6^{+0.2}_{-0.2}$	$0.1^{+0.1}_{-0.1}$
sdM6.0	3000-4.5-1.5	$0.6^{+0.2}_{-0.2}$	$0.3^{+0.4}_{-0.2}$	$1.4^{+0.0}_{-0.0}$	$0.7^{+0.3}_{-0.2}$	$0.4^{+0.2}_{-0.1}$
sdM6.5$^{(*)}$	2900-5.5-0.0	$0.2^{+0.5}_{-0.4}$	$0.4^{+0.6}_{-0.5}$	$0.0^{+0.0}_{-0.0}$	$0.0^{+0.3}_{-0.1}$	$0.0^{+0.2}_{-0.1}$
sdM8.0	2800-5.0-2.5	$0.4^{+0.2}_{-0.2}$	$0.3^{+0.2}_{-0.2}$	$0.7^{+0.0}_{-0.0}$	$0.6^{+0.2}_{-0.2}$	$0.0^{+0.1}_{-0.1}$
sdM9.5	2600-4.5-2.5	$0.6^{+0.2}_{-0.2}$	$0.4^{+0.2}_{-0.2}$	$0.5^{+0.0}_{-0.0}$	$0.8^{+0.2}_{-0.2}$	$0.5^{+0.1}_{-0.1}$
esdM0.0	3600-4.5-1.5	$0.2^{+0.2}_{-0.2}$	$0.4^{+0.2}_{-0.2}$	$0.6^{+0.0}_{-0.0}$	$0.6^{+0.2}_{-0.1}$	$0.3^{+0.1}_{-0.0}$
esdM0.5	3600-4.5-1.5	$0.2^{+0.2}_{-0.2}$	$0.6^{+0.3}_{-0.2}$	$0.5^{+0.0}_{-0.0}$	$0.6^{+0.2}_{-0.1}$	$0.3^{+0.1}_{-0.0}$
esdM1.0	3600-4.5-1.5	$0.3^{+0.2}_{-0.2}$	$0.6^{+0.3}_{-0.3}$	$0.6^{+0.0}_{-0.0}$	$0.7^{+0.2}_{-0.1}$	$0.1^{+0.1}_{-0.0}$
esdM1.5	3400-4.5-1.5	$0.2^{+0.2}_{-0.2}$	$0.4^{+0.3}_{-0.2}$	$0.7^{+0.0}_{-0.0}$	$0.7^{+0.2}_{-0.1}$	$0.4^{+0.1}_{-0.0}$
esdM2.0	3400-4.5-1.5	$0.3^{+0.2}_{-0.2}$	$0.5^{+0.3}_{-0.2}$	$0.8^{+0.0}_{-0.0}$	$0.9^{+0.2}_{-0.1}$	$0.5^{+0.1}_{-0.1}$
esdM3.0	3400-5.0-1.5	$0.2^{+0.2}_{-0.2}$	$0.5^{+0.2}_{-0.2}$	$0.7^{+0.0}_{-0.0}$	$0.9^{+0.2}_{-0.1}$	$0.4^{+0.1}_{-0.1}$
esdM3.5	3400-5.0-1.5	$0.0^{+0.2}_{-0.2}$	$0.4^{+0.2}_{-0.2}$	$0.4^{+0.0}_{-0.0}$	$0.7^{+0.2}_{-0.2}$	$0.2^{+0.1}_{-0.1}$
esdM4.0	3200-4.5-2.0	$0.5^{+0.2}_{-0.2}$	$0.7^{+0.2}_{-0.2}$	$0.4^{+0.0}_{-0.0}$	$0.9^{+0.2}_{-0.2}$	$0.4^{+0.1}_{-0.1}$
esdM4.5	3200-4.5-1.5	$0.6^{+0.2}_{-0.2}$	$0.4^{+0.2}_{-0.2}$	$0.9^{+0.0}_{-0.0}$	$0.8^{+0.2}_{-0.2}$	$0.4^{+0.1}_{-0.1}$
esdM5.0	3200-4.5-1.5	$0.4^{+0.2}_{-0.2}$	$0.7^{+0.3}_{-0.2}$	$0.7^{+0.0}_{-0.0}$	$0.9^{+0.2}_{-0.2}$	$0.5^{+0.1}_{-0.1}$
esdM5.5	3100-4.5-2.0	$0.6^{+0.2}_{-0.2}$	$0.8^{+0.2}_{-0.2}$	$0.8^{+0.0}_{-0.0}$	$1.2^{+0.3}_{-0.3}$	$0.7^{+0.2}_{-0.1}$
esdM6.0	3200-5.0-2.0	$0.1^{+0.2}_{-0.2}$	$0.6^{+0.2}_{-0.2}$	$0.4^{+0.0}_{-0.0}$	$0.8^{+0.2}_{-0.2}$	$0.4^{+0.1}_{-0.1}$
esdM6.5	3100-4.5-2.0	$0.3^{+0.3}_{-0.3}$	$0.7^{+0.2}_{-0.2}$	$0.7^{+0.0}_{-0.0}$	$1.0^{+0.3}_{-0.3}$	$0.4^{+0.1}_{-0.1}$
esdM7.5	3000-5.0-2.0	$0.2^{+0.2}_{-0.2}$	$0.6^{+0.2}_{-0.2}$	$0.7^{+0.0}_{-0.0}$	$0.8^{+0.2}_{-0.2}$	$0.3^{+0.1}_{-0.1}$
esdM8.5	2800-4.5-2.5	$0.4^{+0.2}_{-0.2}$	$0.6^{+0.2}_{-0.2}$	$0.6^{+0.0}_{-0.0}$	$0.8^{+0.3}_{-0.2}$	$0.1^{+0.1}_{-0.1}$
usdM0.0	3500-4.5-2.5	$0.5^{+0.4}_{-0.3}$	$1.2^{+0.5}_{-0.4}$	$1.2^{+0.0}_{-0.0}$	$0.6^{+0.3}_{-0.2}$	$0.2^{+0.2}_{-0.2}$
usdM0.5$^{(*)}$	3600-5.0-2.5	$-0.4^{+0.3}_{-0.2}$	$0.6^{+0.4}_{-0.4}$	$0.4^{+0.0}_{-0.0}$	$0.5^{+0.2}_{-0.2}$	$0.1^{+0.1}_{-0.1}$
usdM1.0	3600-5.0-1.5	$-0.2^{+0.2}_{-0.2}$	$0.6^{+0.4}_{-0.4}$	$0.5^{+0.0}_{-0.0}$	$0.3^{+0.2}_{-0.2}$	$0.2^{+0.1}_{-0.1}$
usdM2.5	3400-4.5-2.0	$0.1^{+0.2}_{-0.2}$	$0.8^{+0.4}_{-0.4}$	$1.0^{+0.0}_{-0.0}$	$0.7^{+0.2}_{-0.2}$	$0.8^{+0.2}_{-0.1}$
usdM3.0	3400-4.5-2.0	$-0.2^{+0.2}_{-0.2}$	$1.2^{+0.4}_{-0.4}$	$0.9^{+0.0}_{-0.0}$	$0.5^{+0.4}_{-0.2}$	$0.3^{+0.1}_{-0.1}$
usdM4.0$^{(*)}$	3500-5.5-2.0	$0.1^{+0.3}_{-0.2}$	$0.8^{+0.4}_{-0.3}$	$0.9^{+0.0}_{-0.0}$	$0.8^{+0.2}_{-0.2}$	$0.5^{+0.1}_{-0.1}$
usdM4.5	3300-5.0-2.0	$-0.1^{+0.3}_{-0.2}$	$0.6^{+0.3}_{-0.2}$	$0.5^{+0.0}_{-0.0}$	$0.5^{+0.2}_{-0.2}$	$0.3^{+0.1}_{-0.1}$
usdM5.0	3400-5.5-2.5	$-0.4^{+0.2}_{-0.2}$	$0.6^{+0.3}_{-0.3}$	$0.6^{+0.0}_{-0.0}$	$0.5^{+0.2}_{-0.2}$	$0.3^{+0.1}_{-0.1}$
usdM6.0	3200-5.0-2.0	$0.1^{+0.2}_{-0.1}$	$1.0^{+0.3}_{-0.3}$	$0.4^{+0.0}_{-0.0}$	$0.6^{+0.1}_{-0.1}$	$0.3^{+0.1}_{-0.1}$
usdM7.5	3000-5.0-2.5	$-0.1^{+0.2}_{-0.2}$	$1.0^{+0.3}_{-0.3}$	$0.4^{+0.1}_{-0.1}$	$0.6^{+0.1}_{-0.1}$	$0.2^{+0.2}_{-0.1}$
usdM8.5	3000-5.5-2.5	$-0.2^{+0.2}_{-0.2}$	$0.8^{+0.3}_{-0.3}$	$0.3^{+0.1}_{-0.1}$	$0.4^{+0.2}_{-0.2}$	$0.0^{+0.2}_{-0.1}$

Notes. Uncertainties are rounded to the nearest integer and given for a change of ±100 K in effective temperature. Targets marked with an asterisk indicate spectra with a low signal-to-noise ratio, whose results must be treated with caution.

We checked the few cases where our best fits suggest solar metallicity. There are four sdMs in this case (including the sdM6.5 specifically treated below) and only one esdM (esdM7.0) also discussed below. For the sdM1.5 we find that the best "FF" fits indicate solar metallicity while the other procedures suggest −0.5 dex. The inspection of the width of the lines (K, Na, Ca) is inconclusive, preventing a decision between one or the other metallicity (Fig. A.13). For the sdM3.0, all four fits are identical and suggest solar metallicity while the third best fit of the
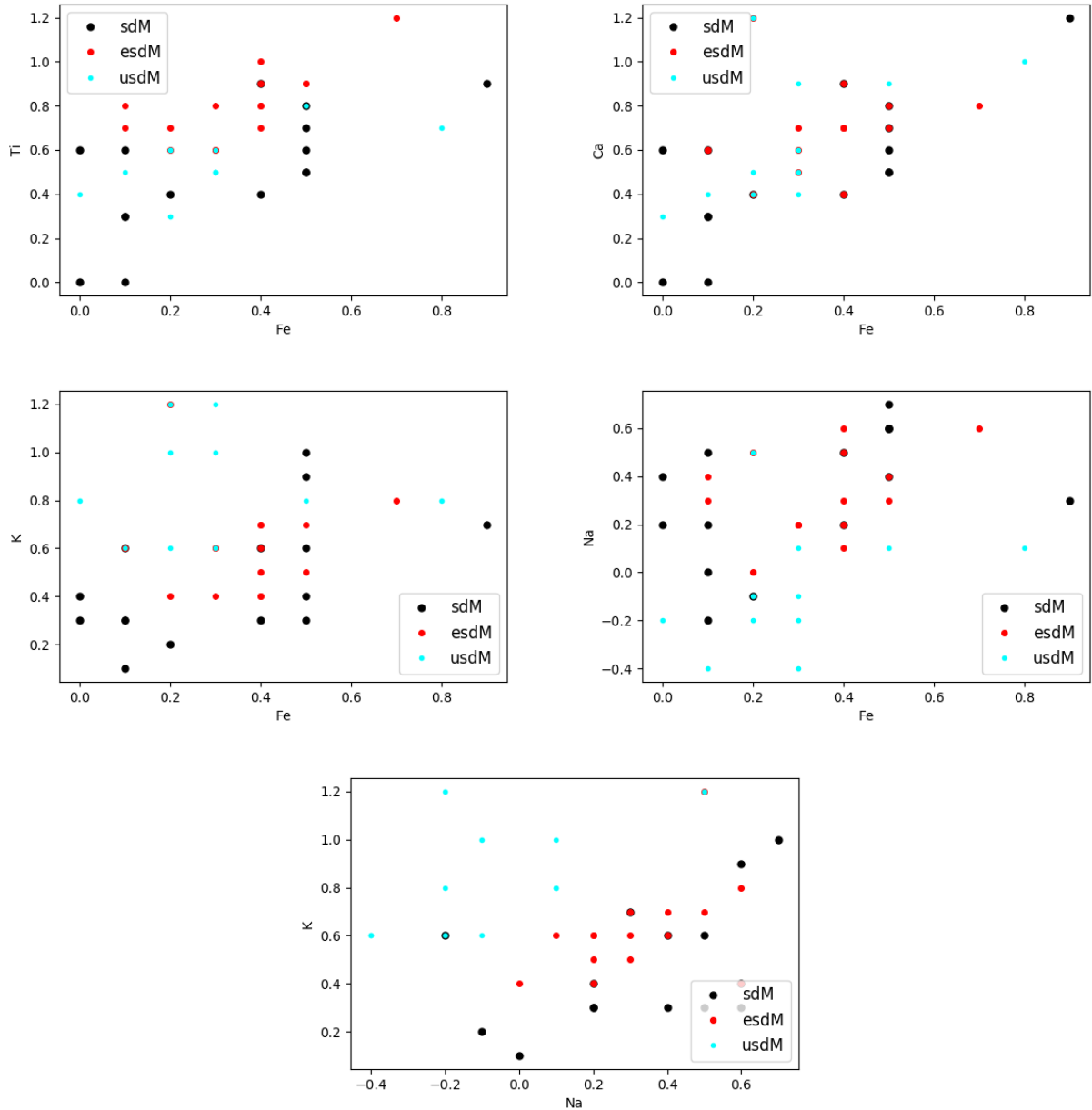
Fig. 4. Scatter in the abundances of sdMs (black symbols), esdMs (red), and usdMs (cyan) for several elements: Fe, Ti, K, Na, and Ca (Table 3).

"FF" procedure yields −0.5 dex. The case of sdM5.0 indicates solar metallicity too but all other fits suggest −0.5 dex, confirmed by the width of the sodium and potassium lines, which advocate metallicity lower than solar with a temperature 3200 K. In the case of these three sdMs, we conclude that they might be peculiar somehow and require further investigation with better-quality data.

We also reviewed the four esdMs (esdM1.0, esdM1.5, esdM2.0, and esdM4.5) with differences of 200 K or more in temperature and ≥1.0 dex in metallicity comparing the four fitting procedures described in Sect. 5.1. We note that the three best fits of the "FF" procedure yield results within the step of the models. Therefore, we inspected the sodium, potassium, and calcium lines where we noticed that the best model fits occurred for the lowest metallicity values in all cases (Fig. A.14).

Finally, we observe four notable outliers discussed below after checking the best fits derived from the different procedures. We emphasise that we obtained one single spectrum per target.

– sdM0.0 is not included in our abundance analysis because the sodium and potassium lines are clearly resolved in our X-shooter spectrum. We confirm this target as a spectroscopic binary, which will be discussed in a separate paper. Any fit to spectral lines and abundance analysis on the spectrum taken at this specific epoch is therefore flawed.

– sdM6.5 (1610−0040) is a known astrometric binary (Koren et al. 2016) with a mix of spectral features typical of both L subdwarfs and solar-type M dwarfs (Lépine et al. 2003; Reiners & Basri 2006; Cushing & Vacca 2006). We derive a temperature of 2900 K with a gravity of 5.5 dex and solar metallicity with a reasonable "FF" model fit (Fig. A.1).

– esdM7.0 shows solar metallicity in the case of the full fitting procedure but lower metallicities with the other three cases. We inspected the sodium, potassium, and calcium lines of this object and conclude that the lines are broader than model predictions at solar metallicity, favouring the metal-poor solution. (Fig. A.14). We note that this object also has a low-quality spectrum.

– usdM3.0 exhibits a large difference when inspecting the best three chi-squared fits using the "FF" procedure, with variations of up to 200 K in temperature and 2.0 dex in metallicity. These differences are larger than any other object in our sample. We inspected the width and depth of the main sodium and potassium lines and find that they appear shallower with a potential double peak, which may indicate binarity (Fig. A.15). However, we obtained one single spectrum for this source so we cannot exclude other phenomenon like rotation, flare activity or spots that can affect our results. A few additional spectra with a minimum spectral resolution of 10000 are required to confirm this possibility, which would explain the large variations in the determination of the physical parameters.

7. Conclusions

Our atlas of VLT/X-shooter 0.45–2.5 μm moderate-resolution spectra represents an important database to classify metal-poor subdwarfs and represents an important resource for future large-scale surveys (WEAVE, 4MOST, LSST; Dalton et al. 2012, 2014; de Jong et al. 2014; Ivezic et al. 2008) and space missions such as the *James Webb* Space Telescope (Gardner et al. 2009) and Euclid (Mellier 2016). We derived radial velocities for all subdwarfs from the shift of the strongest optical lines. We inferred physical parameters (metallicities, temperatures, and gravities) for 43 metal-poor M dwarfs by comparing their SEDs over the 450–2500 nm range to the latest BT-Settl synthetic spectra. The main results of our analysis can be summarised as follows:

– The best gravity range for M subdwarfs is $\log(g) = 5.0$–5.5 dex.

– The metallicities inferred from the BT-Settl models for sdMs, esdMs, and usdMs are −0.5, −1.5, and −2.0 dex with errors of 0.5 dex, respectively.

– The ranges in T_{eff} for sdMs, esdMs, and usdMs are comparable and lie in the intervals 3700–2600 K, 3800–2900 K, and 3700–2900 K with uncertainties of 100 K, respectively.

– The Ca and Ti elements show an over-abundance while Na behaves in an opposite manner when compared to the iron abundance.

Improvements in the determination of the physical parameters and abundances of metal-poor low-mass dwarfs require refined, uniform, and complete model atmosphere grids to improve the fits. More advanced procedures are needed to improve the quality of the fits to observed SEDs treating atomic lines in a self-consistent way, with model atmospheres and spectra computed for one set of input parameters. Models should take into account the enhancement of C/O and improve the modelling of single lines updating abundances of the various elements present in cool atmospheres. To truly determine the physical parameters of M subdwarfs and test evolutionary models at low metallicity, the discovery of metal-poor low-mass transiting eclipsing binaries is key.

References

Adibekyan, V. Z., Sousa, S. G., Santos, N. C., et al. 2012, A&A, 545, A32
Allard, F., & Freytag, B. 2010, Highlights Astron., 15, 756
Allard, F., Baraffe, I., Chabrier, G., & Barman, T. 2003, ESA SP, 539, 247
Allard, F., Allard, N. F., Johnas, C. M. S., et al. 2007, IAU Symp., 240, 332
Allard, F., Homeier, D., & Freytag, B. 2012, Roy. Soc. London Philos. Trans. Ser. A, 370, 2765
Anglada-Escudé, G., Tuomi, M., Gerlach, E., et al. 2013, A&A, 556, A126
Anglada-Escudé, G., Arriagada, P., Tuomi, M., et al. 2014, MNRAS, 443, L89
Asplund, M., Grevesse, N., Sauval, A. J., & Scott, P. 2009, ARA&A, 47, 481
Baraffe, I., Chabrier, G., Allard, F., & Hauschildt, P. H. 1997, A&A, 327, 1054
Baraffe, I., Homeier, D., Allard, F., & Chabrier, G. 2015, A&A, 577, A42
Barber, R. J., Tennyson, J., Harris, G. J., & Tolchenov, R. N. 2006, MNRAS, 368, 1087
Bean, J. L., Sneden, C., Hauschildt, P. H., Johns-Krull, C. M., & Benedict, G. F. 2006, ApJ, 652, 1604
Bessell, M. S. 1991, AJ, 101, 662
Bochanski, J. J., Hawley, S. L., Covey, K. R., et al. 2010, AJ, 139, 2679
Bonfils, X., Delfosse, X., Udry, S., et al. 2005, A&A, 442, 635
Caffau, E., Ludwig, H.-G., Steffen, M., Freytag, B., & Bonifacio, P. 2011, Sol. Phys., 268, 255
Cushing, M. C., & Vacca, W. D. 2006, AJ, 131, 1797
Dalton, G., Trager, S. C., Abrams, D. C., et al. 2012, Proc. SPIE, 8446, 84460P
Dalton, G., Trager, S. C., Abrams, D. C., et al. 2014, Proc. SPIE, 9147, 91470L
de Bruijne, J. H. J. 2012, Astrophys. Space. Sci., 341, 31
de Jong, R. S., Barden, S., Bellido-Tirado, O., et al. 2014, Proc. SPIE, 9147, 91470M
Delfosse, X., Bonfils, X., Forveille, T., et al. 2013, A&A, 553, A8
Dittmann, J. A., Irwin, J. M., Charbonneau, D., & Newton, E. R. 2016, ApJ, 818, 153
D'Odorico, S., Dekker, H., Mazzoleni, R., et al. 2006, Proc. SPIE, 6269
Feroz, F., & Hobson, M. P. 2014, MNRAS, 437, 3540
Francois, P. 1986, A&A, 160, 264
Freytag, B., Steffen, M., Wedemeyer-Böhm, S., et al. 2010, Astrophysics Source Code Library [record ascl:1011.014]
Fuhrmann, K., Axer, M., & Gehren, T. 1995, A&A, 301, 492
Gardner, J. P., Mather, J. C., Clampin, M., et al. 2009, Astrophys. Space Sci. Proc., 10, 1
Gizis, J. E. 1997, AJ, 113, 806
Gratton, R. G., & Sneden, C. 1994, A&A, 287, 927
Hejazi, N., De Robertis, M. M., & Dawson, P. C. 2015, AJ, 149, 140
Henry, T. J., Jao, W.-C., Subasavage, J. P., et al. 2006, AJ, 132, 2360
Ivezic, Z., Axelrod, T., Brandt, W. N., et al. 2008, Serb. Astron. J., 176, 1
Jao, W.-C., Henry, T. J., Beaulieu, T. D., & Subasavage, J. P. 2008, AJ, 136, 840
Jofré, P., Heiter, U., Soubiran, C., et al. 2014, A&A, 564, A133
Johnson, J. A., & Apps, K. 2009, ApJ, 699, 933
Kausch, W., Noll, S., Smette, A., et al. 2015, A&A, 576, A78
Kesseli, A. Y., West, A. A., Veyette, M., et al. 2017, ApJS, 230, 16
Kirkpatrick, J. D., Reid, I. N., Liebert, J., et al. 1999, ApJ, 519, 802
Kirkpatrick, J. D., Gelino, C. R., Cushing, M. C., et al. 2012, ApJ, 753, 156
Kirkpatrick, J. D., Schneider, A., Fajardo-Acosta, S., et al. 2014, ApJ, 783, 122

Koren, S. C., Blake, C. H., Dahn, C. C., & Harris, H. C. 2016, AJ, 151, 57
Kupka, F., Piskunov, N., Ryabchikova, T. A., Stempels, H. C., & Weiss, W. W. 1999, A&AS, 138, 119
Lépine, S., Rich, R. M., & Shara, M. M. 2003, ApJ, 591, L49
Leggett, S. K., Allard, F., Berriman, G., Dahn, C. C., & Hauschildt, P. H. 1996, ApJS, 104, 117
Leggett, S. K., Allard, F., Dahn, C., et al. 2000, ApJ, 535, 965
Lépine, S., Rich, R. M., & Shara, M. M. 2007, ApJ, 669, 1235
Lindgren, S., Heiter, U., & Seifahrt, A. 2016, A&A, 586, A100
Lodieu, N., Espinoza Contreras, M., Zapatero Osorio, M. R., et al. 2017, A&A, 598, A92
Mellier, Y. 2016, COSPAR Meeting, Vol. 41, 41st COSPAR Scientific Assembly, Abstracts from the Meeting that was to be held 30 July – 7 August at the Istanbul Congress Center (ICC), Turkey, but was cancelled. See http://cospar2016.tubitak.gov.tr/en/, Abstract H0.2-1-16
Monteiro, H., Jao, W.-C., Henry, T., Subasavage, J., & Beaulieu, T. 2006, ApJ, 638, 446
Morton, T. D., Bryson, S. T., Coughlin, J. L., et al. 2016, ApJ, 822, 86
Muirhead, P. S., Hamren, K., Schlawin, E., et al. 2012, ApJ, 750, L37
Neves, V., Bonfils, X., Santos, N. C., et al. 2012, A&A, 538, A25
Neves, V., Bonfils, X., Santos, N. C., et al. 2013, A&A, 551, A36
Neves, V., Bonfils, X., Santos, N. C., et al. 2014, A&A, 568, A121
Newton, E. R., Charbonneau, D., Irwin, J., & Mann, A. W. 2015, ApJ, 800, 85
Nissen, P. E., Gustafsson, B., Edvardsson, B., & Gilmore, G. 1994, A&A, 285, 440
Nutzman, P., & Charbonneau, D. 2008, PASP, 120, 317
Önehag, A., Heiter, U., Gustafsson, B., et al. 2012, A&A, 542, A33
Pavlenko, Y. V. 1997, Ap&SS, 253, 43
Pavlenko, Y. V. 2014, Astron. Rep., 58, 825
Pavlenko, Y. V., Zhang, Z. H., Gálvez-Ortiz, M. C., Kushniruk, I. O., & Jones, H. R. A. 2015, A&A, 582, A92
Plez, B. 1998, A&A, 337, 495
Plez, B. 2008, Phys. Scr. Vol. T, 133, 014003
Quirrenbach, A., Amado, P. J., Seifert, W., et al. 2012, Proc. SPIE, 8446, 84460R
Rajpurohit, A. S., Reylé, C., Allard, F., et al. 2013, A&A, 556, A15
Rajpurohit, A. S., Reylé, C., Allard, F., et al. 2014, A&A, 564, A90
Rajpurohit, A. S., Reyle, C., Allard, F., et al. 2016, A&A, 596, A33
Reiners, A., & Basri, G. 2006, AJ, 131, 1806
Robertson, P., Roy, A., & Mahadevan, S. 2015, ApJ, 805, L22
Rojas-Ayala, B., Covey, K. R., Muirhead, P. S., & Lloyd, J. P. 2010, ApJ, 720, L113
Rojas-Ayala, B., Covey, K. R., Muirhead, P. S., & Lloyd, J. P. 2012, ApJ, 748, 93
Ryabchikova, T. A., Pakhomov, Y. V., & Piskunov, N. E. 2011, Kazan Izdatel Kazanskogo Universiteta, 153, 61
Savcheva, A. S., West, A. A., & Bochanski, J. J. 2014, ApJ, 794, 145
Schlaufman, K. C., & Laughlin, G. 2010, A&A, 519, A105
Scholz, R.-D., Heber, U., Heuser, C., et al. 2015, A&A, 574, A96
Smette, A., Sana, H., Noll, S., et al. 2015, A&A, 576, A77
Sozzetti, A., Giacobbe, P., Lattanzi, M. G., et al. 2014, MNRAS, 437, 497
Steiner, O., Vigeesh, G., Krieger, L., et al. 2007, Astron. Nachr., 328, 323
Terrien, R. C., Mahadevan, S., Bender, C. F., et al. 2012, ApJ, 747, L38
Testi, L. 2009, A&A, 503, 639
Tody, D. 1986, Proc. SPIE, 627, 733
Tody, D. 1993, ASP Conf. Ser., 52, 173
Vernet, J., Dekker, H., D'Odorico, S., et al. 2011, A&A, 536, A105
Woolf, V. M., & Wallerstein, G. 2005, MNRAS, 356, 963
Woolf, V. M., & Wallerstein, G. 2006, PASP, 118, 218
Woolf, V. M., Lépine, S., & Wallerstein, G. 2009, PASP, 121, 117
Zhang, Z. H., Pinfield, D. J., Gálvez-Ortiz, M. C., et al. 2017, MNRAS, 464, 3040

Appendix A: Model fit to VLT/X-shooter spectra
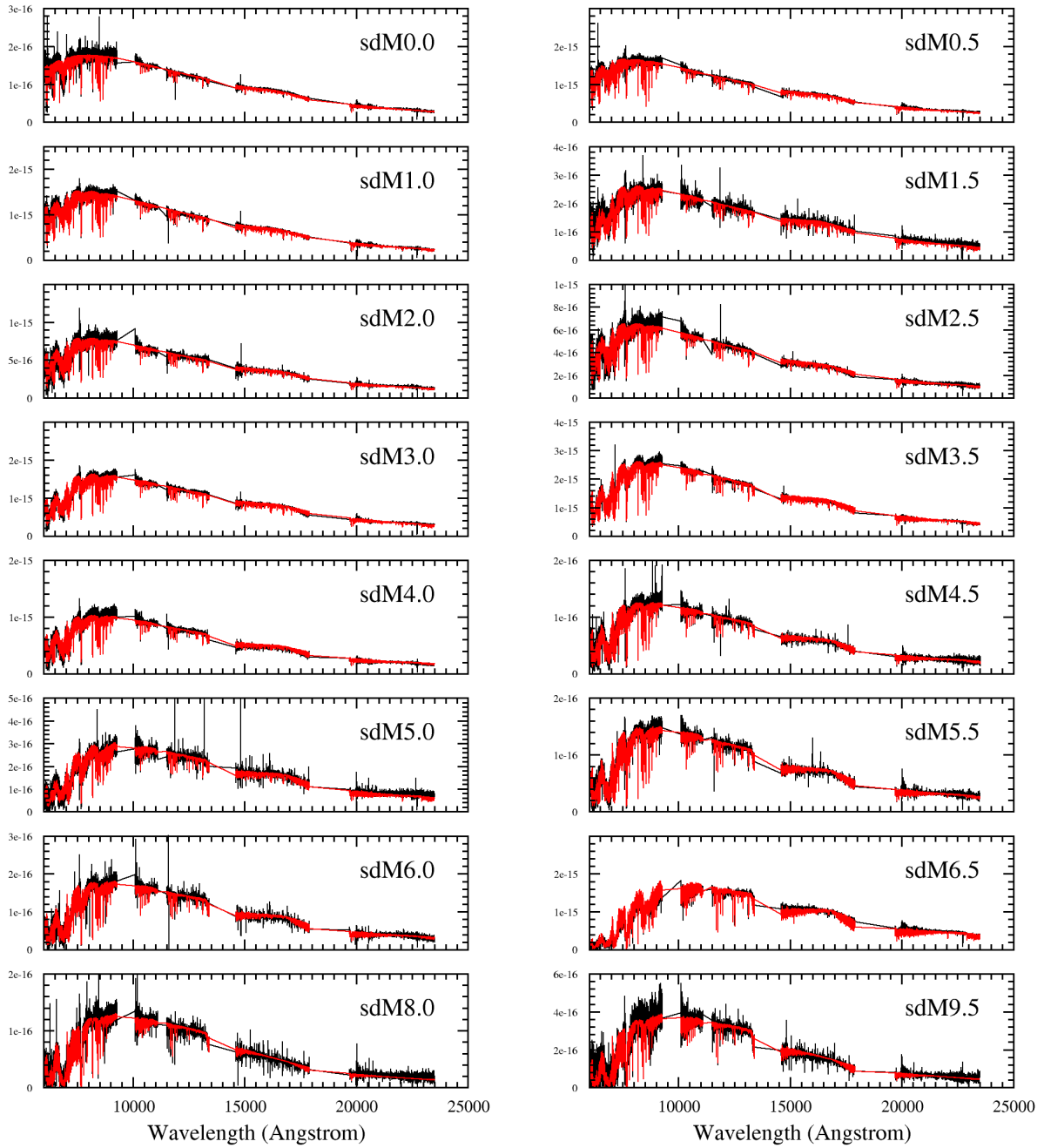
Fig. A.1. VLT/X-shooter UVB (450–550 nm), VIS (550–1000 nm) and NIR (1000–2500 nm) spectra of sdMs with spectral types from M0.0 to M9.5 (black lines) compared with the best BT-Settl spectra smoothed to the observed spectra. Spectral types are quoted in the top right corner for each subtype. The fits shown are for the FF case.
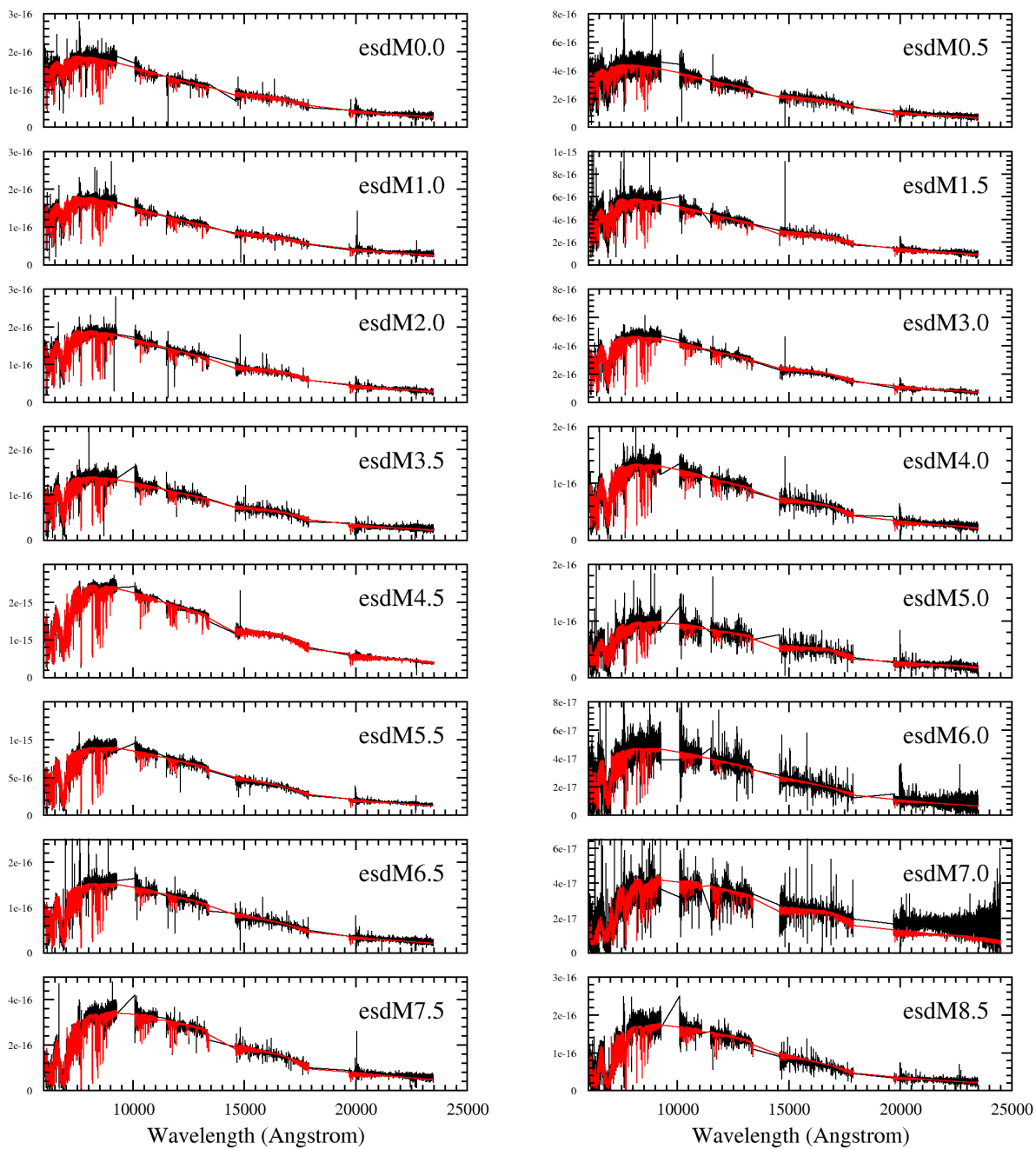
Fig. A.2. Same as Fig. A.1 for esdMs.
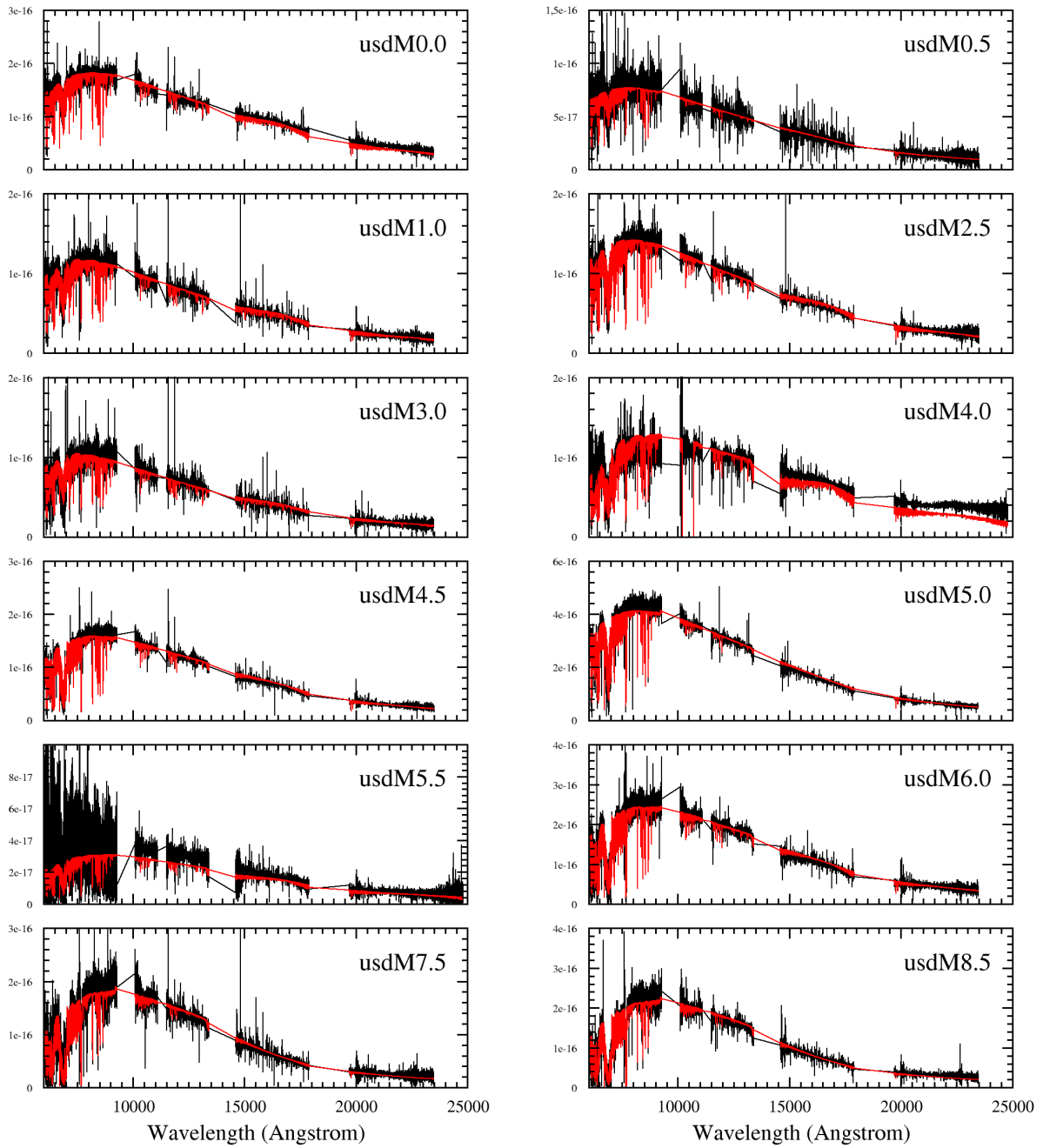
Fig. A.3. Same as Fig. A.1 for usdMs.
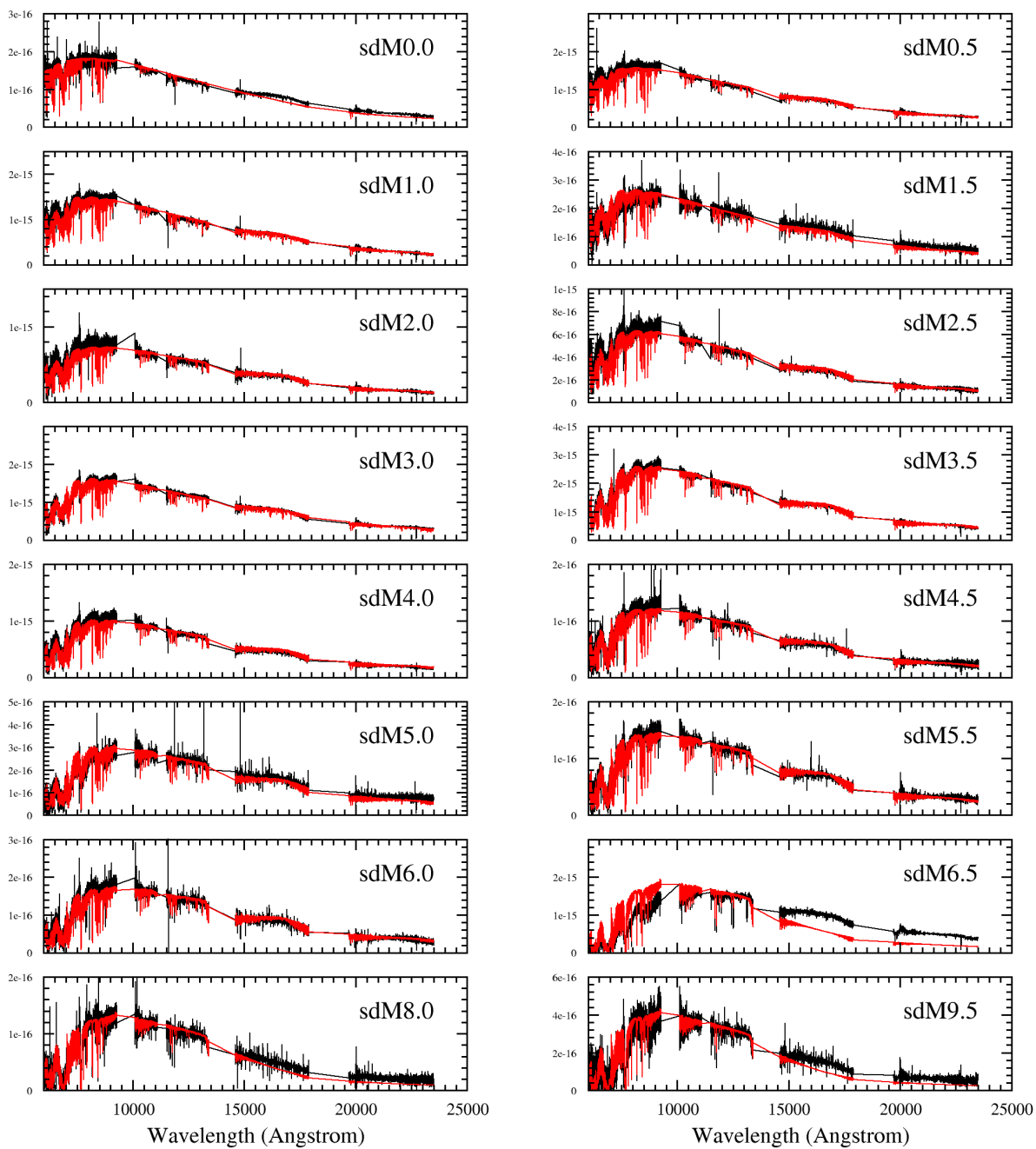
Fig. A.4. VLT/X-shooter UVB (450–550 nm), VIS (550–1000 nm) and NIR (1000–2500 nm) spectra of sdMs with spectral types from M0.0 to M9.5 (black lines) compared with the best BT-Settl spectra smoothed to the observed spectra. Spectral types are quoted in the top right corner for each subtype. The fits shown are for the LL case.
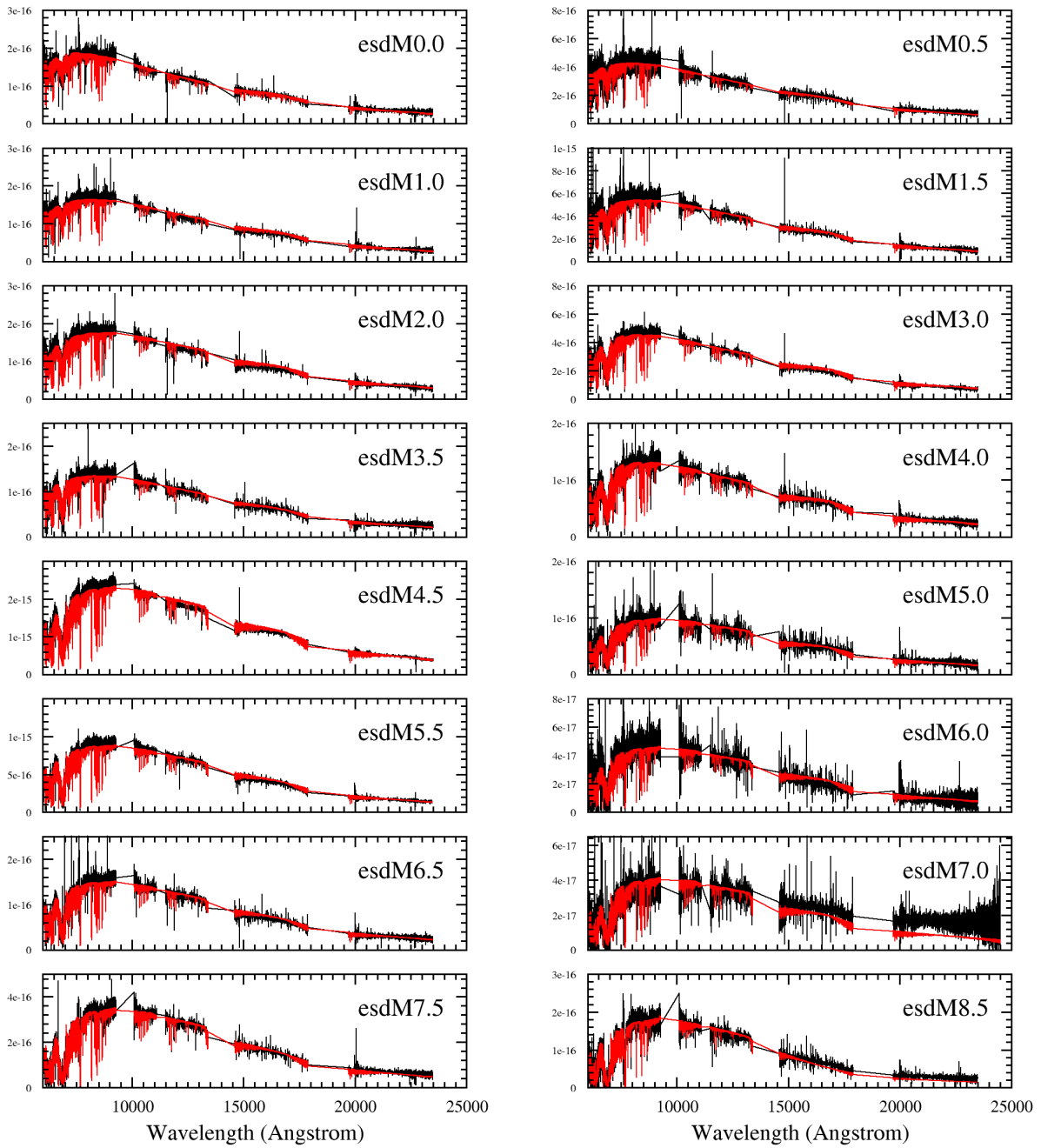
Fig. A.5. Same as Fig. A.4 for esdMs.
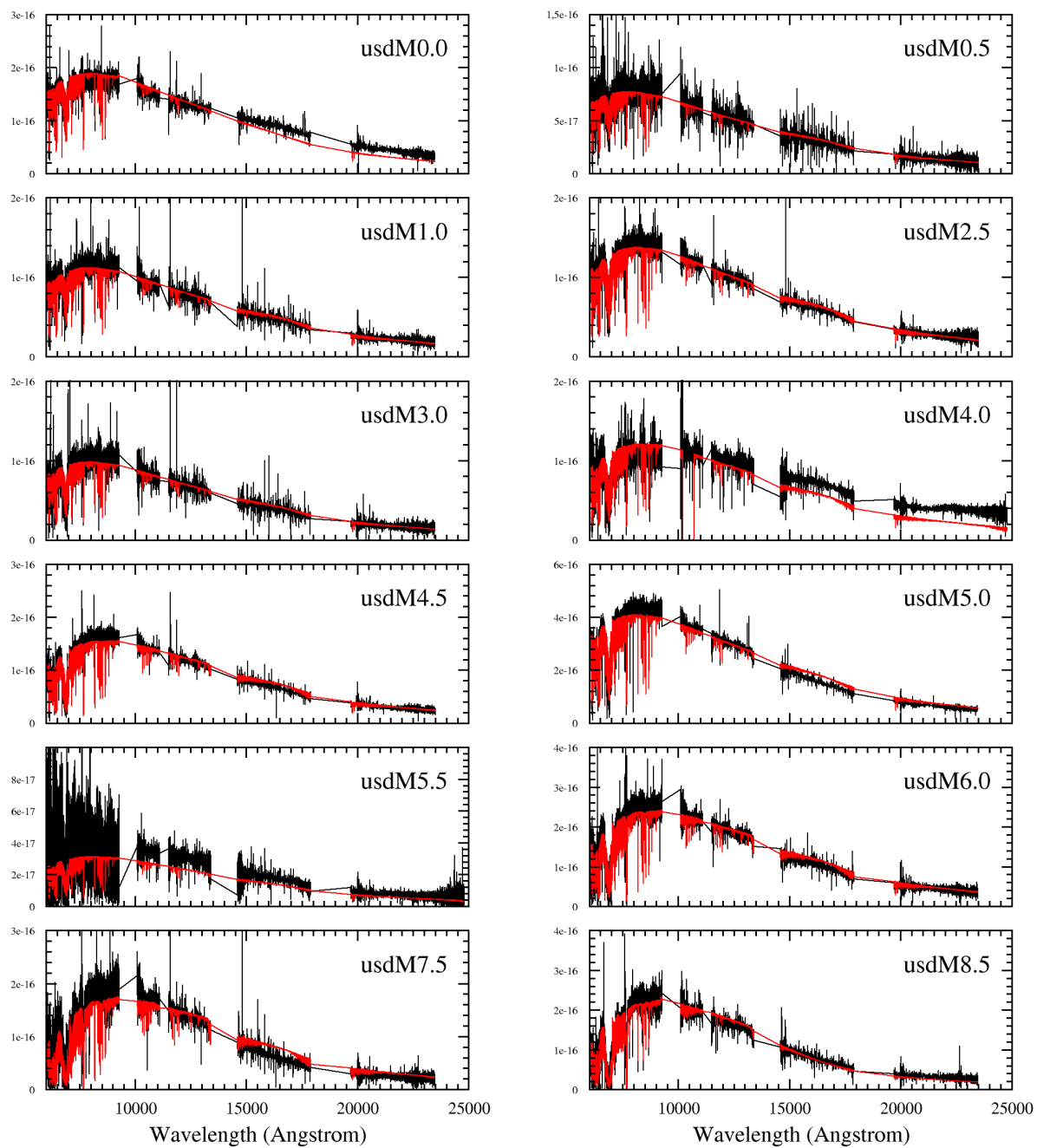
Fig. A.6. Same as Fig. A.4 for usdMs.
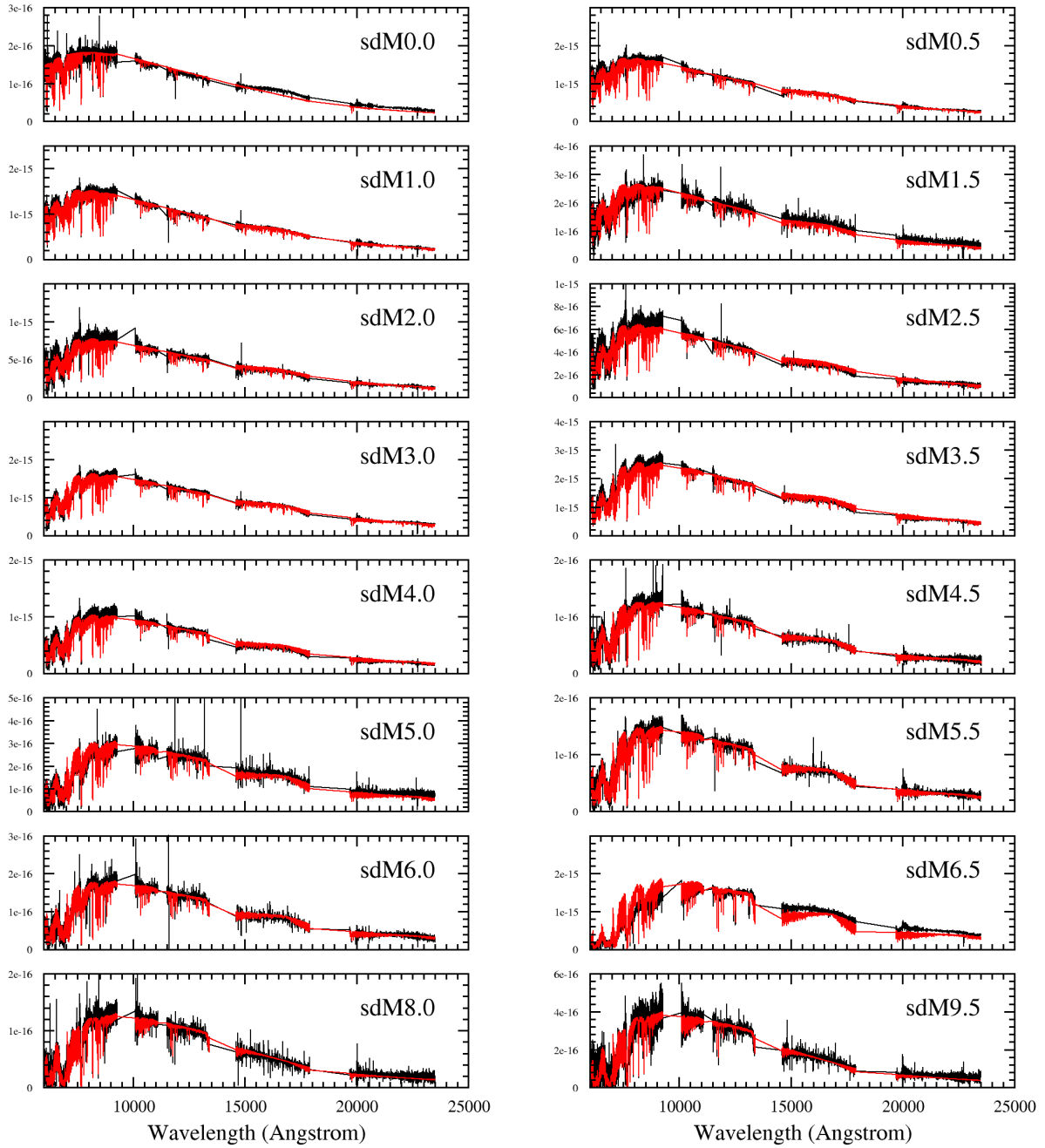
Fig. A.7. VLT/X-shooter UVB (450–550 nm), VIS (550–1000 nm) and NIR (1000–2500 nm) spectra of sdMs with spectral types from M0.0 to M9.5 (black lines) compared with the best BT-Settl spectra smoothed to the observed spectra. Spectral types are quoted in the top right corner for each subtype. The fits shown are for the FL case.
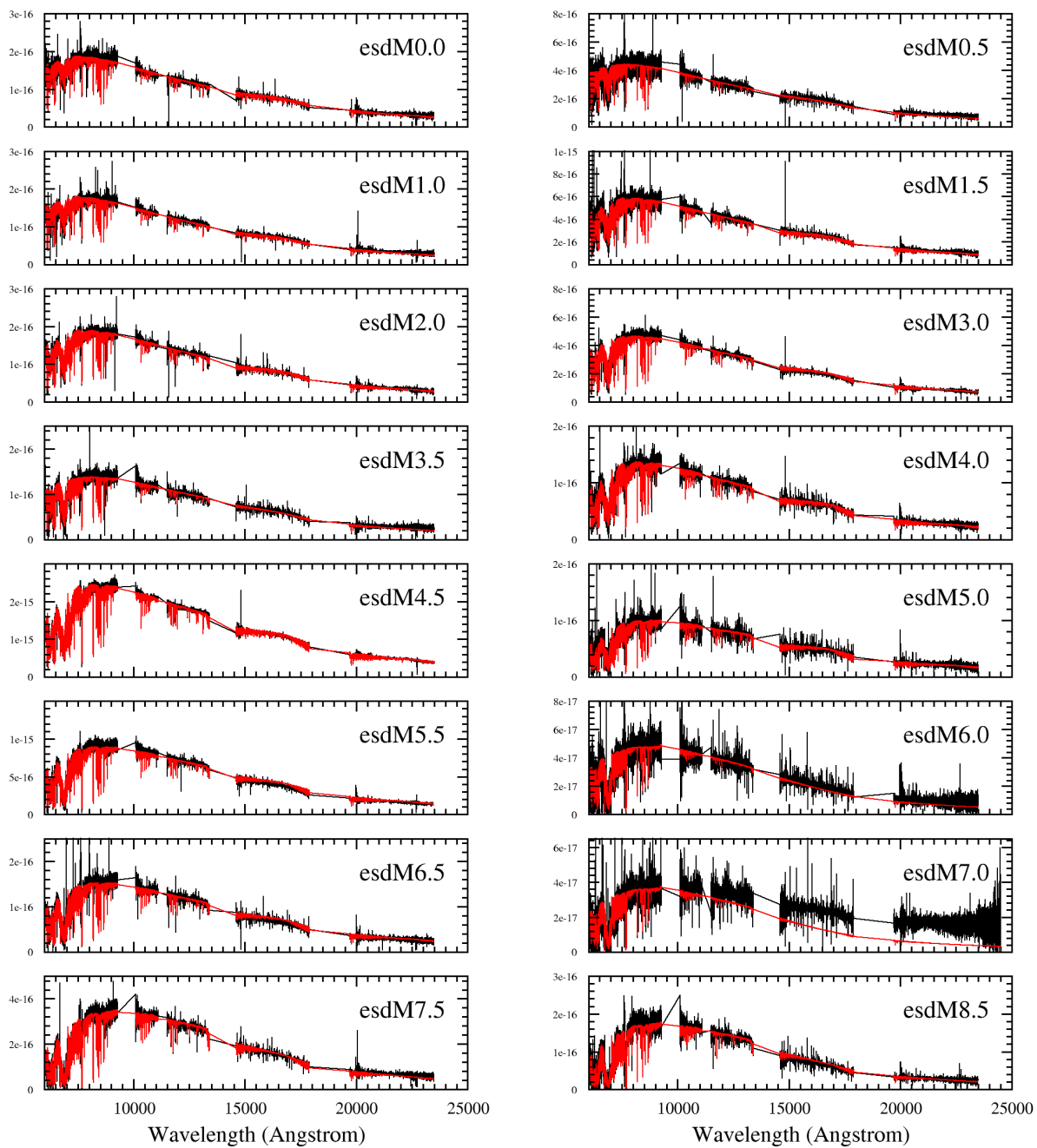
Fig. A.8. Same as Fig. A.7 for esdMs.
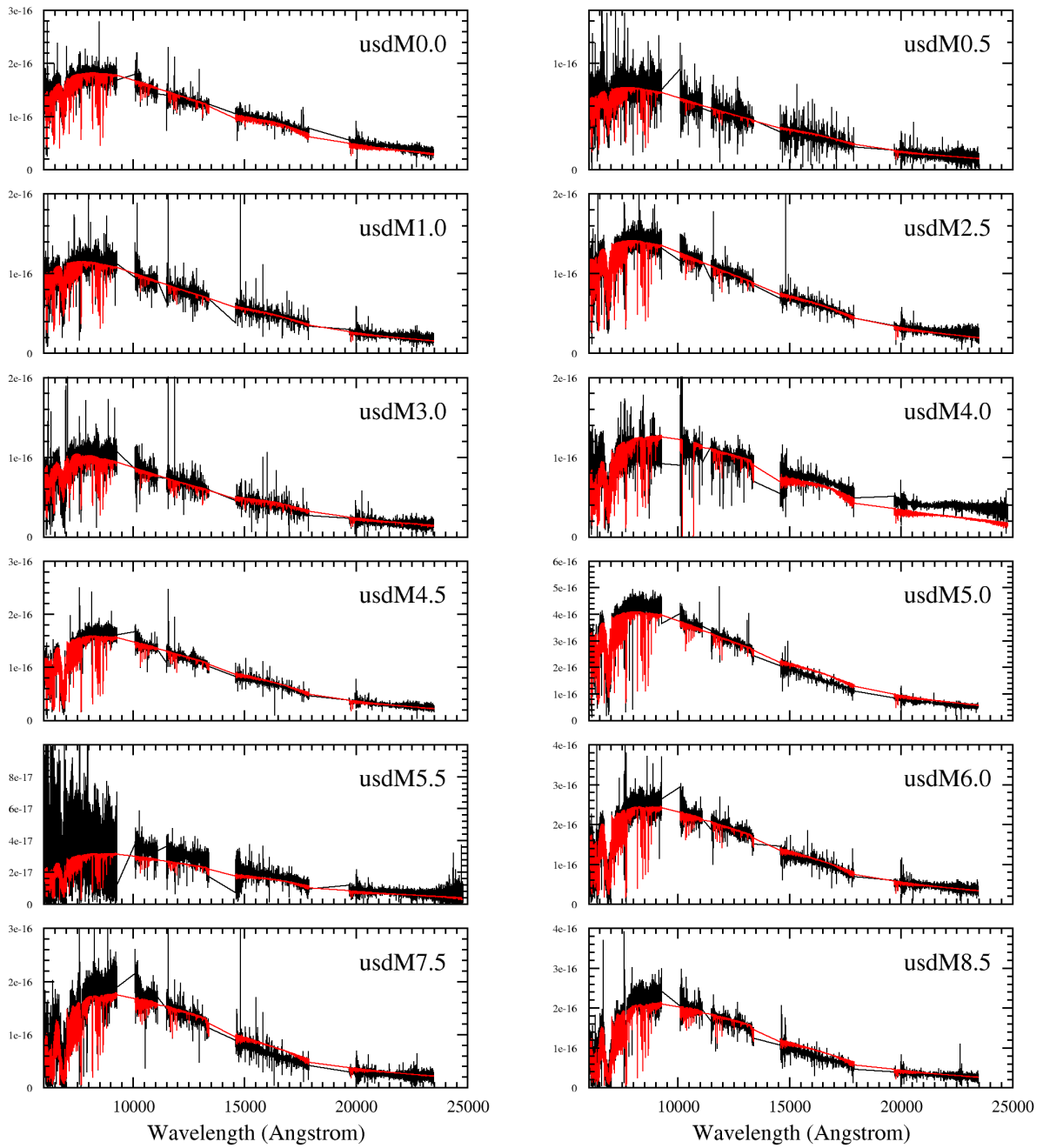
Fig. A.9. Same as Fig. A.7 for usdMs.
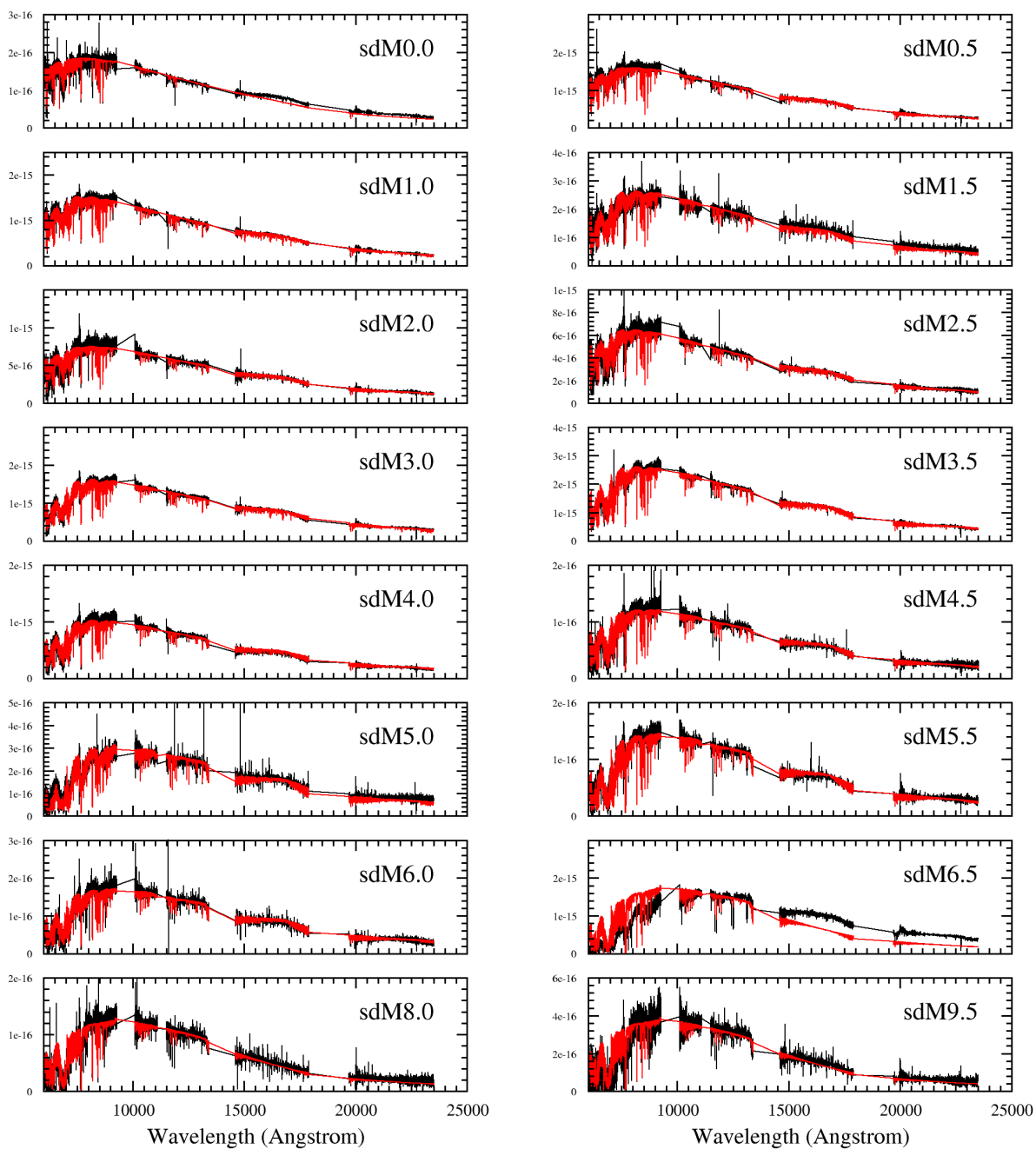
Fig. A.10. VLT/X-shooter UVB (450–550 nm), VIS (550–1000 nm) and NIR (1000–2500 nm) spectra of sdMs with spectral types from M0.0 to M9.5 (black lines) compared with the best BT-Settl spectra smoothed to the observed spectra. Spectral types are quoted in the top right corner for each subtype. The fits shown are for the LF case.
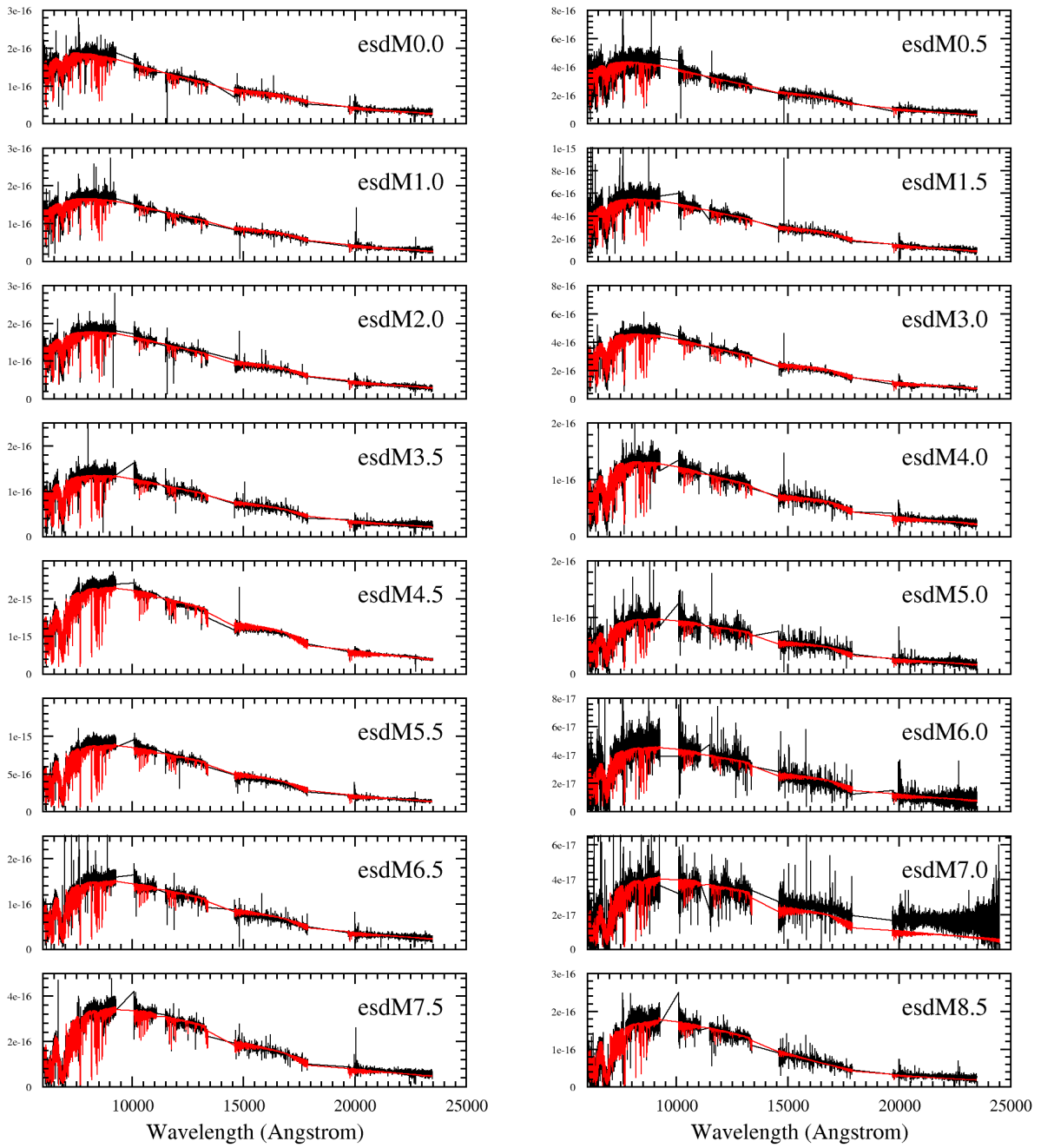
Fig. A.11. Same as Fig. A.10 for esdMs.
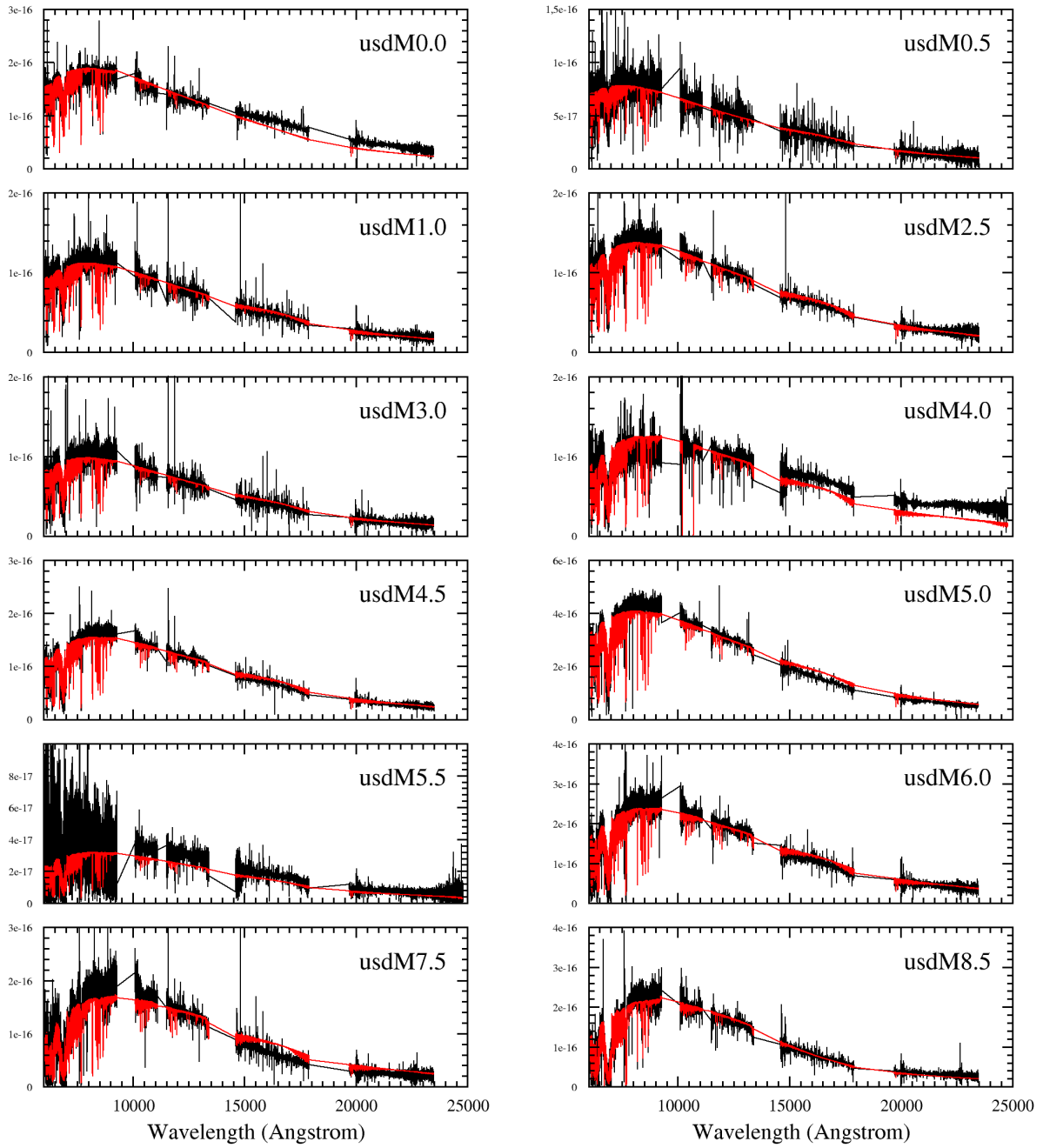
Fig. A.12. Same as Fig. A.10 for usdMs.
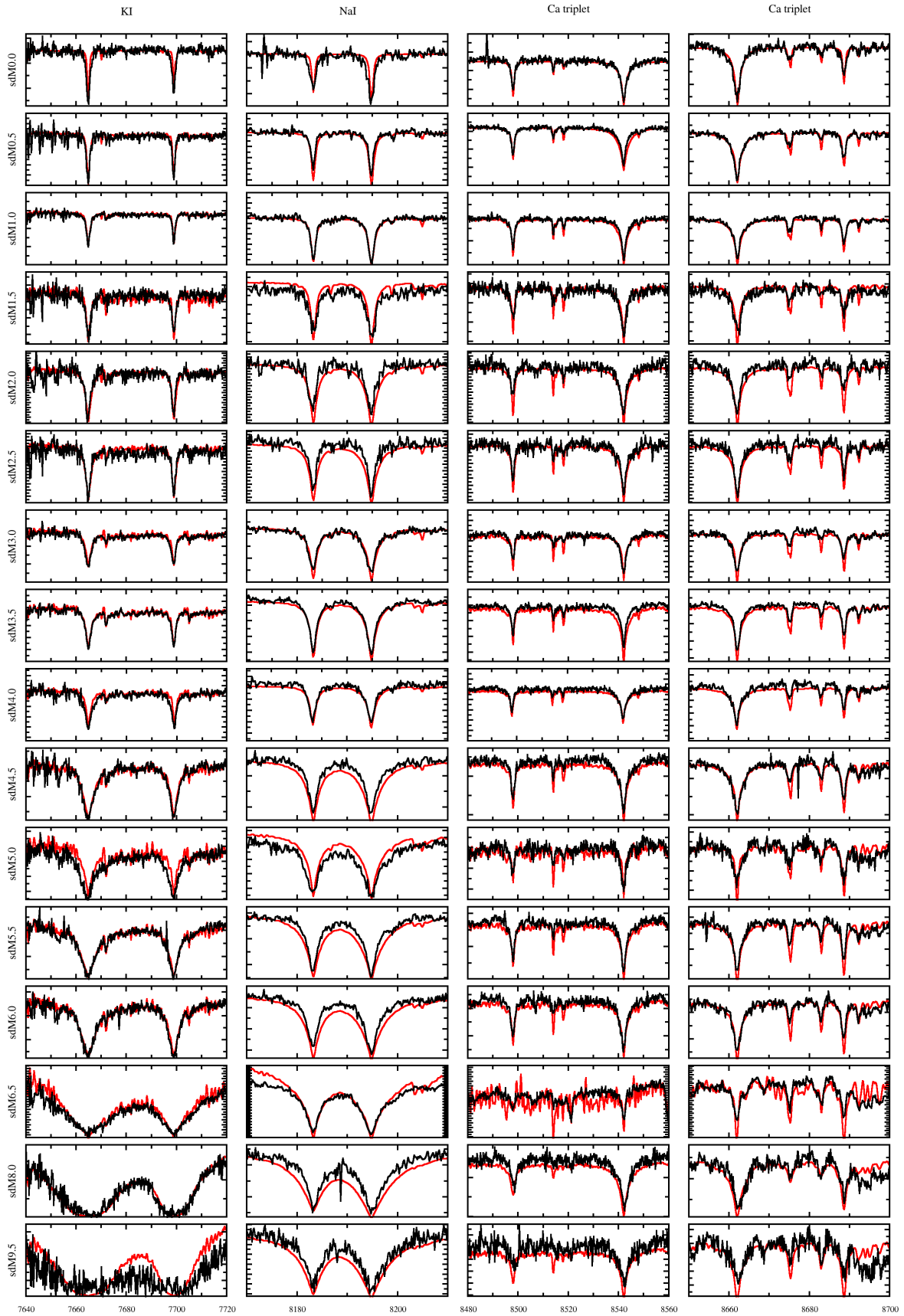
Fig. A.13. VLT/X-shooter UVB (450–550 nm), VIS (550–1000 nm) and NIR (1000–2500 nm) spectra of sdMs with spectral types from M0.0 to M9.5 (black lines) compared with the best BT-Settl spectra smoothed to the observed spectra for a few strong lines (sodium, potassium, and calcium). Spectral types are quoted in the top right corner for each subtype.

Fig. A.14. Same as Fig. A.13 for esdMs.

Fig. A.15. Same as Fig. A.13 for usdMs.

Appendix B: Tables with physical parameters of subdwarfs

Table B.1. Derived physical parameters for sdMs, esdMs, and usdMs from the comparison between the observed X-shooter spectra and the BT-Settl synthetic spectra using the "FF" procedure.

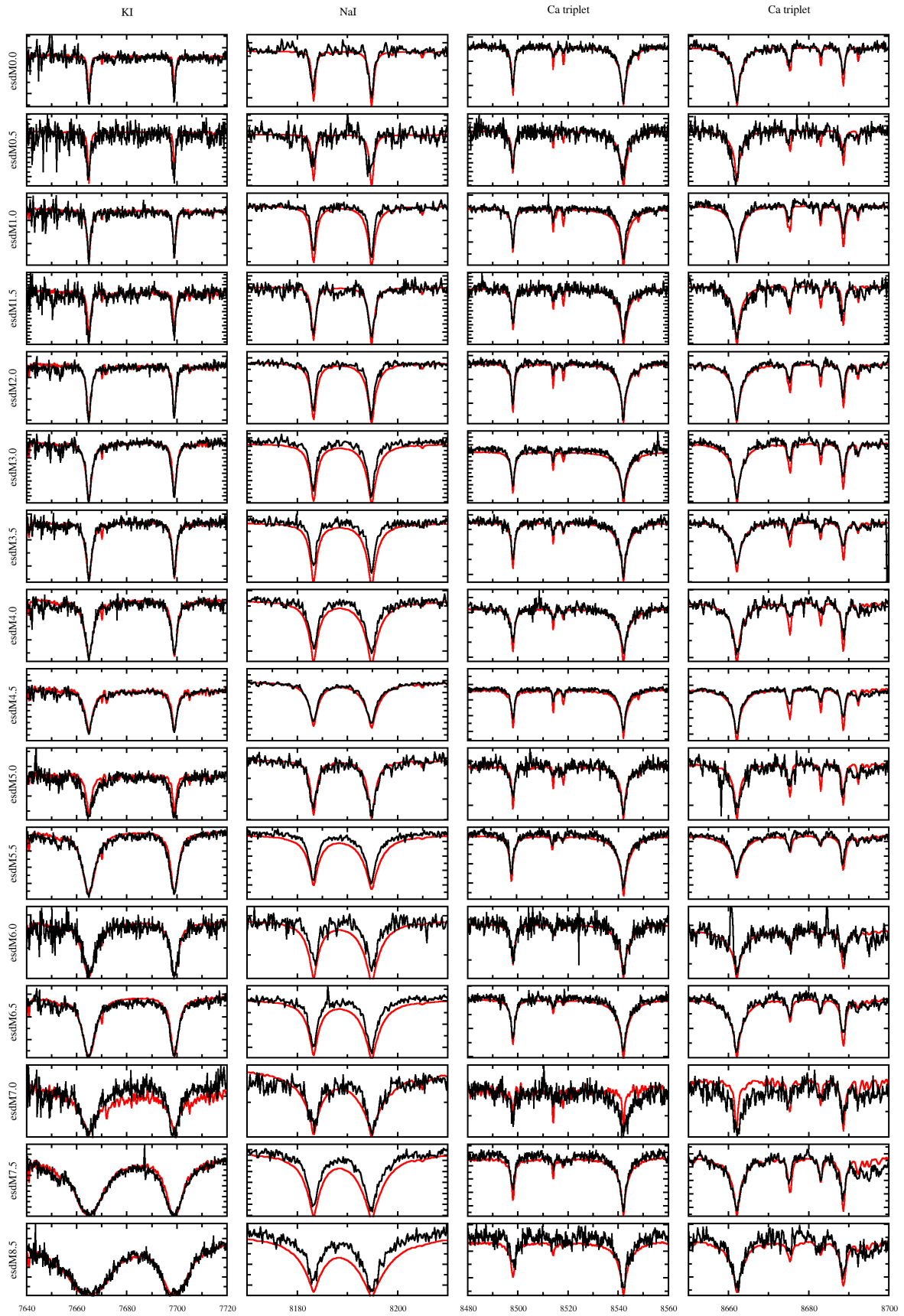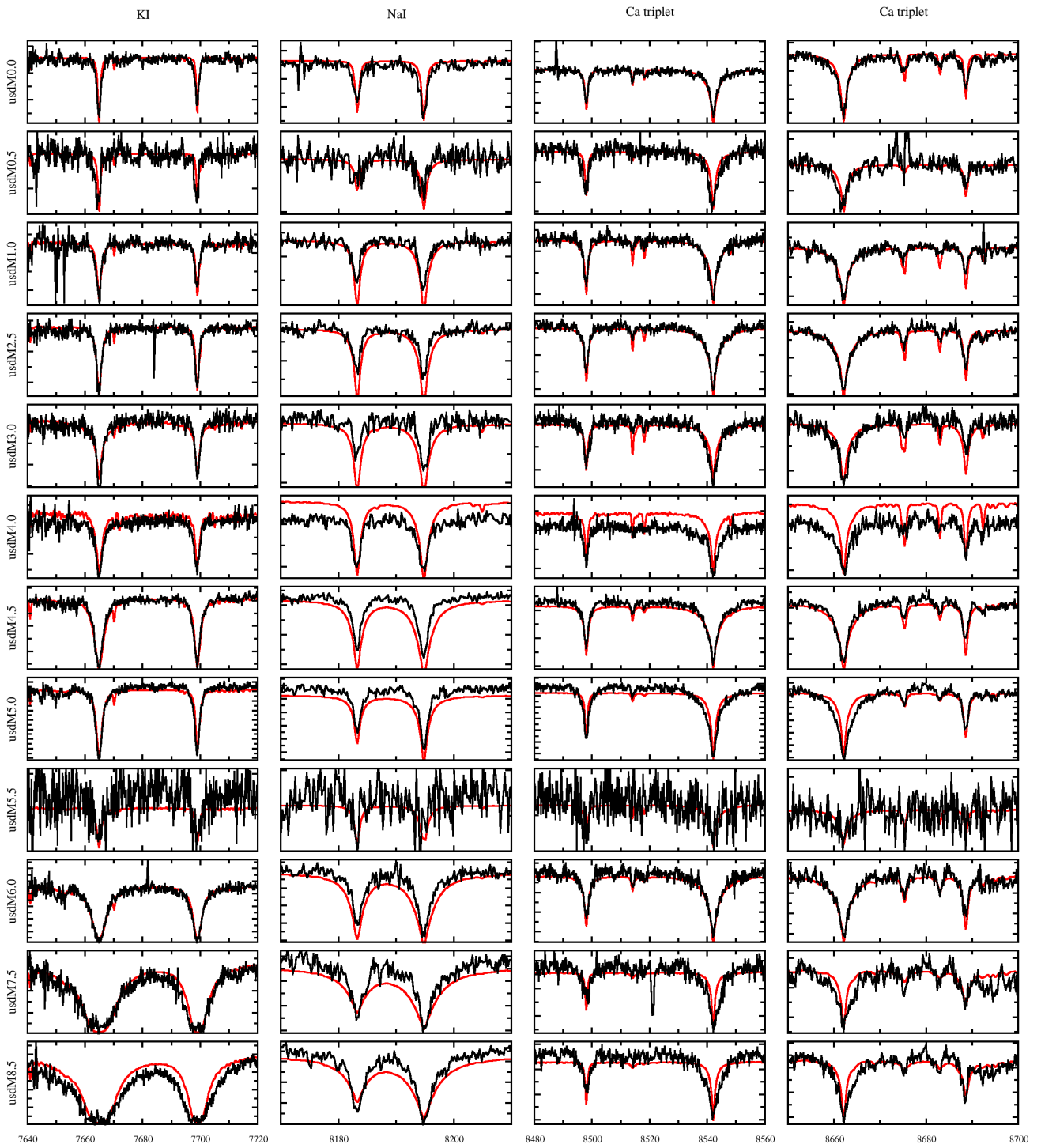| SpT	Range	$T_{\rm eff}$	$\log g$	M/H	chi^2	Factor	Model
sdM0.0	FF	3600	4.5	−2.0	1.336	2.263e-22	lte036.0-4.5-2.0a+0.4.BT-Settl.spec.7.dat
sdM0.5	FF	3700	5.0	−1.0	72.07	1.782e-21	lte037.0-5.0-1.0a+0.4.BT-Settl.spec.7.dat
sdM1.0	FF	3700	5.0	−0.5	67.22	1.609e-21	lte037.0-5.0-0.5a+0.2.BT-Settl.spec.7.dat
sdM1.5	FF	3600	4.5	−0.0	66.4	3.168e-22	lte036.0-4.5-0.0a+0.0.BT-Settl.spec.7.dat
sdM2.0	FF	3600	5.5	−0.5	46.01	9.281e-22	lte036.0-5.5-0.5a+0.2.BT-Settl.spec.7.dat
sdM2.5	FF	3600	5.5	−0.5	35.09	7.689e-22	lte036.0-5.5-0.5a+0.2.BT-Settl.spec.7.dat
sdM3.0	FF	3500	5.0	−0.0	88.51	2.208e-21	lte035.0-5.0-0.0a+0.0.BT-Settl.spec.7.dat
sdM3.5	FF	3400	5.0	−0.5	161.6	3.916e-21	lte034.0-5.0-0.5a+0.2.BT-Settl.spec.7.dat
sdM4.0	FF	3400	5.0	−1.0	58.22	1.54e-21	lte034.0-5.0-1.0a+0.4.BT-Settl.spec.7.dat
sdM4.5	FF	3300	5.5	−1.0	59.07	2.072e-22	lte033.0-5.5-1.0a+0.4.BT-Settl.spec.7.dat
sdM5.0	FF	3200	5.0	−0.0	62.52	5.826e-22	lte032.0-5.0-0.0a+0.0.BT-Settl.spec.7.dat
sdM5.5	FF	3200	5.5	−1.0	60.94	2.764e-22	lte032.0-5.5-1.0a+0.4.BT-Settl.spec.7.dat
sdM6.0	FF	3200	5.5	−1.0	52.62	3.327e-22	lte032.0-5.5-1.0a+0.4.BT-Settl.spec.7.dat
sdM6.5	FF	2900	5.5	−0.0	828.4	4.589e-21	lte029.0-5.5-0.0a+0.0.BT-Settl.spec.7.dat
sdM8.0	FF	2900	5.5	−2.0	49.54	3.094e-22	lte029.0-5.5-2.0a+0.4.BT-Settl.spec.7.dat
sdM9.5	FF	2800	5.0	−2.0	26.84	1.071e-21	lte028.0-5.0-2.0a+0.4.BT-Settl.spec.7.dat
esdM0.0	FF	3800	5.0	−1.0	46.36	1.789e-22	lte038.0-5.0-1.0a+0.4.BT-Settl.spec.7.dat
esdM0.5	FF	3700	5.0	−1.5	28.12	4.847e-22	lte037.0-5.0-1.5a+0.4.BT-Settl.spec.7.dat
esdM1.0	FF	3800	5.5	−0.5	50.66	1.683e-22	lte038.0-5.5-0.5a+0.2.BT-Settl.spec.7.dat
esdM1.5	FF	3600	5.0	−1.0	24.61	6.996e-22	lte036.0-5.0-1.0a+0.4.BT-Settl.spec.7.dat
esdM2.0	FF	3600	5.5	−1.0	54.63	2.229e-22	lte036.0-5.5-1.0a+0.4.BT-Settl.spec.7.dat
esdM3.0	FF	3500	5.5	−1.5	82.5	6.294e-22	lte035.0-5.5-1.5a+0.4.BT-Settl.spec.7.dat
esdM3.5	FF	3500	5.5	−1.5	38	1.883e-22	lte035.0-5.5-1.5a+0.4.BT-Settl.spec.7.dat
esdM4.0	FF	3400	5.5	−1.5	53.24	2.04e-22	lte034.0-5.5-1.5a+0.4.BT-Settl.spec.7.dat
esdM4.5	FF	3400	5.5	−1.0	260.6	3.594e-21	lte034.0-5.5-1.0a+0.4.BT-Settl.spec.7.dat
esdM5.0	FF	3200	4.5	−1.5	39.72	1.952e-22	lte032.0-4.5-1.5a+0.4.BT-Settl.spec.7.dat
esdM5.5	FF	3300	5.5	−2.0	87.47	1.533e-21	lte033.0-5.5-2.0a+0.4.BT-Settl.spec.7.dat
esdM6.0	FF	3300	5.5	−2.0	27.35	8.065e-23	lte033.0-5.5-2.0a+0.4.BT-Settl.spec.7.dat
esdM6.5	FF	3300	5.5	−2.0	84.99	2.61e-22	lte033.0-5.5-2.0a+0.4.BT-Settl.spec.7.dat
esdM7.0	FF	3200	5.5	−0.0	8.431	8.349e-23	lte032.0-5.5-0.0a+0.0.BT-Settl.spec.7.dat
esdM7.5	FF	3000	5.0	−2.0	75.73	8.239e-22	lte030.0-5.0-2.0a+0.4.BT-Settl.spec.7.dat
esdM8.5	FF	3000	5.5	−2.0	46.61	3.916e-22	lte030.0-5.5-2.0a+0.4.BT-Settl.spec.7.dat
usdM0.0	FF	3500	4.5	−2.0	81.52	2.637e-22	lte035.0-4.5-2.0a+0.4.BT-Settl.spec.7.dat
usdM0.5	FF	3700	5.5	−2.5	35.49	8.444e-23	lte037.0-5.5-2.5a+0.4.BT-Settl.spec.7.dat
usdM1.0	FF	3700	5.5	−1.0	34.9	1.245e-22	lte037.0-5.5-1.0a+0.4.BT-Settl.spec.7.dat
usdM2.5	FF	3600	5.5	−1.5	40.94	1.724e-22	lte036.0-5.5-1.5a+0.4.BT-Settl.spec.7.dat
usdM3.0	FF	3800	6.0	−0.5	40.92	9.605e-23	lte038.0-6.0-0.5a+0.2.BT-Settl.spec.7.dat
usdM4.0	FF	3200	4.5	−1.5	8.887	2.545e-22	lte032.0-4.5-1.5a+0.4.BT-Settl.spec.7.dat
usdM4.5	FF	3400	5.5	−2.0	79.52	2.428e-22	lte034.0-5.5-2.0a+0.4.BT-Settl.spec.7.dat
usdM5.0	FF	3500	5.5	−2.5	128.5	5.667e-22	lte035.0-5.5-2.5a+0.4.BT-Settl.spec.7.dat
usdM5.5	FF	3300	4.5	−2.0	12.52	5.669e-23	lte033.0-4.5-2.0a+0.4.BT-Settl.spec.7.dat
usdM6.0	FF	3300	5.5	−2.0	40.62	4.176e-22	lte033.0-5.5-2.0a+0.4.BT-Settl.spec.7.dat
usdM7.5	FF	3100	5.5	−2.5	25.7	3.749e-22	lte031.0-5.5-2.5a+0.4.BT-Settl.spec.7.dat
usdM8.5	FF	3100	5.5	−2.5	49.69	4.503e-22	lte031.0-5.5-2.5a+0.4.BT-Settl.spec.7.dat

Notes. For each spectral subtype and metal class, we list the best fits with effective temperature ($T_{\rm eff}$), gravity ($\log g$), metallicity (M/H), chi^2 value, factor, and the name of the model.

Table B.2. Derived physical parameters for sdMs, esdMs, and usdMs from the comparison between the observed X-shooter spectra and the BT-Settl synthetic spectra using the "LL" procedure.

SpT	Range	T_{eff}	log g	M/H	chi^2	Factor	Model
sdM0.0	LL	3600	5.5	−2.5	1.274	2.182e-22	lte036.0-5.5-2.5a+0.4.BT-Settl.spec.7.dat
sdM0.5	LL	3500	4.5	−1.5	65.2	2.303e-21	lte035.0-4.5-1.5a+0.4.BT-Settl.spec.7.dat
sdM1.0	LL	3600	5.0	−0.5	44.52	1.843e-21	lte036.0-5.0-0.5a+0.2.BT-Settl.spec.7.dat
sdM1.5	LL	3600	5.0	−0.5	53.5	2.944e-22	lte036.0-5.0-0.5a+0.2.BT-Settl.spec.7.dat
sdM2.0	LL	3300	4.5	−1.5	54.06	1.418e-21	lte033.0-4.5-1.5a+0.4.BT-Settl.spec.7.dat
sdM2.5	LL	3400	5.0	−1.0	33.27	1.013e-21	lte034.0-5.0-1.0a+0.4.BT-Settl.spec.7.dat
sdM3.0	LL	3500	5.0	−0.0	86.06	2.228e-21	lte035.0-5.0-0.0a+0.0.BT-Settl.spec.7.dat
sdM3.5	LL	3300	5.0	−1.0	100	4.559e-21	lte033.0-5.0-1.0a+0.4.BT-Settl.spec.7.dat
sdM4.0	LL	3300	5.0	−1.0	43	1.854e-21	lte033.0-5.0-1.0a+0.4.BT-Settl.spec.7.dat
sdM4.5	LL	3200	5.0	−1.5	64.01	2.467e-22	lte032.0-5.0-1.5a+0.4.BT-Settl.spec.7.dat
sdM5.0	LL	3200	5.5	−0.5	64.17	5.346e-22	lte032.0-5.5-0.5a+0.2.BT-Settl.spec.7.dat
sdM5.5	LL	3100	5.0	−1.5	62.38	3.231e-22	lte031.0-5.0-1.5a+0.4.BT-Settl.spec.7.dat
sdM6.0	LL	3000	4.5	−1.5	68.92	4.55e-22	lte030.0-4.5-1.5a+0.4.BT-Settl.spec.7.dat
sdM6.5	LL	2600	4.5	−2.5	360.4	4.65e-21	lte026.0-4.5-2.5a+0.4.BT-Settl.spec.7.dat
sdM8.0	LL	2800	5.0	−2.5	68.93	3.399e-22	lte028.0-5.0-2.5a+0.4.BT-Settl.spec.7.dat
sdM9.5	LL	2700	5.0	−2.5	33.25	1.083e-21	lte027.0-5.0-2.5a+0.4.BT-Settl.spec.7.dat
esdM0.0	LL	3800	5.0	−1.0	52.51	1.807e-22	lte038.0-5.0-1.0a+0.4.BT-Settl.spec.7.dat
esdM0.5	LL	3600	5.0	−2.0	36.42	5.423e-22	lte036.0-5.0-2.0a+0.4.BT-Settl.spec.7.dat
esdM1.0	LL	3500	4.5	−2.0	43.43	2.508e-22	lte035.0-4.5-2.0a+0.4.BT-Settl.spec.7.dat
esdM1.5	LL	3400	4.5	−2.0	32.73	9.175e-22	lte034.0-4.5-2.0a+0.4.BT-Settl.spec.7.dat
esdM2.0	LL	3300	4.5	−2.0	41.6	3.457e-22	lte033.0-4.5-2.0a+0.4.BT-Settl.spec.7.dat
esdM3.0	LL	3400	5.0	−1.5	54.27	7.476e-22	lte034.0-5.0-1.5a+0.4.BT-Settl.spec.7.dat
esdM3.5	LL	3400	5.0	−2.0	30.57	2.211e-22	lte034.0-5.0-2.0a+0.4.BT-Settl.spec.7.dat
esdM4.0	LL	3300	5.0	−1.5	60.87	2.371e-22	lte033.0-5.0-1.5a+0.4.BT-Settl.spec.7.dat
esdM4.5	LL	3100	4.5	−2.0	188.1	5.634e-21	lte031.0-4.5-2.0a+0.4.BT-Settl.spec.7.dat
esdM5.0	LL	3100	4.5	−2.0	36.16	2.286e-22	lte031.0-4.5-2.0a+0.4.BT-Settl.spec.7.dat
esdM5.5	LL	3200	5.0	−2.0	65.67	1.831e-21	lte032.0-5.0-2.0a+0.4.BT-Settl.spec.7.dat
esdM6.0	LL	3100	4.5	−2.0	29.34	1.116e-22	lte031.0-4.5-2.0a+0.4.BT-Settl.spec.7.dat
esdM6.5	LL	3200	5.0	−2.0	62.31	3.104e-22	lte032.0-5.0-2.0a+0.4.BT-Settl.spec.7.dat
esdM7.0	LL	3000	4.5	−2.0	2.347	9.268e-23	lte030.0-4.5-2.0a+0.4.BT-Settl.spec.7.dat
esdM7.5	LL	3000	5.0	−2.0	93.43	8.48e-22	lte030.0-5.0-2.0a+0.4.BT-Settl.spec.7.dat
esdM8.5	LL	2900	5.0	−2.5	54.67	4.499e-22	lte029.0-5.0-2.5a+0.4.BT-Settl.spec.7.dat
usdM0.0	LL	3600	5.5	−2.5	52.74	2.186e-22	lte036.0-5.5-2.5a+0.4.BT-Settl.spec.7.dat
usdM0.5	LL	3700	5.5	−2.0	52.29	8.588e-23	lte037.0-5.5-2.0a+0.4.BT-Settl.spec.7.dat
usdM1.0	LL	3600	5.0	−2.0	38.42	1.449e-22	lte036.0-5.0-2.0a+0.4.BT-Settl.spec.7.dat
usdM2.5	LL	3500	5.0	−2.0	35.32	1.999e-22	lte035.0-5.0-2.0a+0.4.BT-Settl.spec.7.dat
usdM3.0	LL	3600	5.5	−2.0	38.99	1.27e-22	lte036.0-5.5-2.0a+0.4.BT-Settl.spec.7.dat
usdM4.0	LL	3400	5.0	−2.0	0.7288	1.663e-22	lte034.0-5.0-2.0a+0.4.BT-Settl.spec.7.dat
usdM4.5	LL	3300	5.0	−2.0	81.28	2.949e-22	lte033.0-5.0-2.0a+0.4.BT-Settl.spec.7.dat
usdM5.0	LL	3500	5.5	−2.0	91.84	5.981e-22	lte035.0-5.5-2.0a+0.4.BT-Settl.spec.7.dat
usdM5.5	LL	3500	5.5	−2.0	11.58	3.992e-23	lte035.0-5.5-2.0a+0.4.BT-Settl.spec.7.dat
usdM6.0	LL	3200	5.0	−2.0	44.5	5.027e-22	lte032.0-5.0-2.0a+0.4.BT-Settl.spec.7.dat
usdM7.5	LL	3000	5.0	−2.0	39.86	4.725e-22	lte030.0-5.0-2.0a+0.4.BT-Settl.spec.7.dat
usdM8.5	LL	3000	5.5	−2.5	60.58	5.247e-22	lte030.0-5.5-2.5a+0.4.BT-Settl.spec.7.dat

Table B.3. Derived physical parameters for sdMs, esdMs, and usdMs from the comparison between the observed X-shooter spectra and the BT-Settl synthetic spectra using the "FL" procedure.

SpT	Range	T_{eff}	log g	M/H	chi^2	Factor	Model
sdM0.0	FL	3600	5.5	−2.5	1.274	2.182e-22	lte036.0-5.5-2.5a+0.4.BT-Settl.spec.7.dat
sdM0.5	FL	3700	5.0	−0.5	67.14	1.791e-21	lte037.0-5.0-0.5a+0.2.BT-Settl.spec.7.dat
sdM1.0	FL	3700	5.0	−0.5	45.51	1.627e-21	lte037.0-5.0-0.5a+0.2.BT-Settl.spec.7.dat
sdM1.5	FL	3600	5.0	−0.5	53.5	2.944e-22	lte036.0-5.0-0.5a+0.2.BT-Settl.spec.7.dat
sdM2.0	FL	3600	5.0	−0.0	60.82	9.902e-22	lte036.0-5.0-0.0a+0.0.BT-Settl.spec.7.dat
sdM2.5	FL	3600	5.0	−0.0	35.7	8.194e-22	lte036.0-5.0-0.0a+0.0.BT-Settl.spec.7.dat
sdM3.0	FL	3500	5.0	−0.0	86.06	2.228e-21	lte035.0-5.0-0.0a+0.0.BT-Settl.spec.7.dat
sdM3.5	FL	3400	5.0	−0.0	102.6	4.24e-21	lte034.0-5.0-0.0a+0.0.BT-Settl.spec.7.dat
sdM4.0	FL	3400	5.0	−0.5	49.18	1.64e-21	lte034.0-5.0-0.5a+0.2.BT-Settl.spec.7.dat
sdM4.5	FL	3300	5.5	−1.0	65.18	2.143e-22	lte033.0-5.5-1.0a+0.4.BT-Settl.spec.7.dat
sdM5.0	FL	3200	5.5	−0.5	64.17	5.346e-22	lte032.0-5.5-0.5a+0.2.BT-Settl.spec.7.dat
sdM5.5	FL	3200	5.5	−1.0	64.82	2.837e-22	lte032.0-5.5-1.0a+0.4.BT-Settl.spec.7.dat
sdM6.0	FL	3200	5.5	−1.0	71.23	3.416e-22	lte032.0-5.5-1.0a+0.4.BT-Settl.spec.7.dat
sdM6.5	FL	2900	5.5	−1.0	457.5	3.619e-21	lte029.0-5.5-1.0a+0.4.BT-Settl.spec.7.dat
sdM8.0	FL	2900	5.5	−2.0	70.63	3.246e-22	lte029.0-5.5-2.0a+0.4.BT-Settl.spec.7.dat
sdM9.5	FL	2800	5.5	−2.0	36.7	1.048e-21	lte028.0-5.5-2.0a+0.4.BT-Settl.spec.7.dat
esdM0.0	FL	3800	5.0	−1.0	52.51	1.807e-22	lte038.0-5.0-1.0a+0.4.BT-Settl.spec.7.dat
esdM0.5	FL	3700	5.5	−2.0	36.68	4.752e-22	lte037.0-5.5-2.0a+0.4.BT-Settl.spec.7.dat
esdM1.0	FL	3800	5.5	−1.0	51.58	1.689e-22	lte038.0-5.5-1.0a+0.4.BT-Settl.spec.7.dat
esdM1.5	FL	3600	5.5	−1.0	35.37	6.833e-22	lte036.0-5.5-1.0a+0.4.BT-Settl.spec.7.dat
esdM2.0	FL	3600	5.5	−1.0	48.16	2.251e-22	lte036.0-5.5-1.0a+0.4.BT-Settl.spec.7.dat
esdM3.0	FL	3500	5.5	−1.5	61.37	6.495e-22	lte035.0-5.5-1.5a+0.4.BT-Settl.spec.7.dat
esdM3.5	FL	3500	5.5	−2.0	34.19	1.914e-22	lte035.0-5.5-2.0a+0.4.BT-Settl.spec.7.dat
esdM4.0	FL	3400	5.5	−1.0	67.85	2.034e-22	lte034.0-5.5-1.0a+0.4.BT-Settl.spec.7.dat
esdM4.5	FL	3400	5.5	−1.0	211.3	3.624e-21	lte034.0-5.5-1.0a+0.4.BT-Settl.spec.7.dat
esdM5.0	FL	3200	5.0	−1.5	40.53	1.967e-22	lte032.0-5.0-1.5a+0.4.BT-Settl.spec.7.dat
esdM5.5	FL	3300	5.5	−1.5	74.79	1.598e-21	lte033.0-5.5-1.5a+0.4.BT-Settl.spec.7.dat
esdM6.0	FL	3300	5.5	−2.5	31.14	8.05e-23	lte033.0-5.5-2.5a+0.4.BT-Settl.spec.7.dat
esdM6.5	FL	3300	5.5	−1.5	72.68	2.71e-22	lte033.0-5.5-1.5a+0.4.BT-Settl.spec.7.dat
esdM7.0	FL	3200	5.5	−2.5	2.51	6.41e-23	lte032.0-5.5-2.5a+0.4.BT-Settl.spec.7.dat
esdM7.5	FL	3000	5.0	−2.0	93.43	8.48e-22	lte030.0-5.0-2.0a+0.4.BT-Settl.spec.7.dat
esdM8.5	FL	3000	5.5	−2.0	54.82	4.189e-22	lte030.0-5.5-2.0a+0.4.BT-Settl.spec.7.dat
usdM0.0	FL	3500	4.5	−2.0	54.08	2.592e-22	lte035.0-4.5-2.0a+0.4.BT-Settl.spec.7.dat
usdM0.5	FL	3700	5.5	−2.0	52.29	8.588e-23	lte037.0-5.5-2.0a+0.4.BT-Settl.spec.7.dat
usdM1.0	FL	3700	5.5	−2.0	38.67	1.27e-22	lte037.0-5.5-2.0a+0.4.BT-Settl.spec.7.dat
usdM2.5	FL	3600	5.5	−2.0	35.69	1.745e-22	lte036.0-5.5-2.0a+0.4.BT-Settl.spec.7.dat
usdM3.0	FL	3800	5.5	−0.5	46.05	1.005e-22	lte038.0-5.5-0.5a+0.2.BT-Settl.spec.7.dat
usdM4.0	FL	3200	4.5	−2.0	0.772	2.22e-22	lte032.0-4.5-2.0a+0.4.BT-Settl.spec.7.dat
usdM4.5	FL	3400	5.5	−2.0	85.36	2.539e-22	lte034.0-5.5-2.0a+0.4.BT-Settl.spec.7.dat
usdM5.0	FL	3500	5.5	−2.0	91.84	5.981e-22	lte035.0-5.5-2.0a+0.4.BT-Settl.spec.7.dat
usdM5.5	FL	3300	5.0	−2.0	11.84	5.247e-23	lte033.0-5.0-2.0a+0.4.BT-Settl.spec.7.dat
usdM6.0	FL	3300	5.5	−2.0	47.7	4.314e-22	lte033.0-5.5-2.0a+0.4.BT-Settl.spec.7.dat
usdM7.5	FL	3100	5.5	−2.0	40.37	4.046e-22	lte031.0-5.5-2.0a+0.4.BT-Settl.spec.7.dat
usdM8.5	FL	3100	5.5	−2.0	72.9	4.879e-22	lte031.0-5.5-2.0a+0.4.BT-Settl.spec.7.dat

Notes. For each spectral subtype and metal class, we list the best fits with effective temperature (T_{eff}), gravity (log g), metallicity (M/H), chi^2 value, factor, and the name of the model.

Table B.4. Derived physical parameters for sdMs, esdMs, and usdMs from the comparison between the observed X-shooter spectra and the BT-Settl synthetic spectra using the "LF" procedure.

SpT	Range	T_{eff}	log g	M/H	chi^2	Factor	Model
sdM0.0	LF	3700	5.5	−2.5	3.692	2.021e-22	lte037.0-5.5-2.5a+0.4.BT-Settl.spec.7.dat
sdM0.5	LF	3600	4.5	−1.5	87.73	1.999e-21	lte036.0-4.5-1.5a+0.4.BT-Settl.spec.7.dat
sdM1.0	LF	3700	5.0	−0.5	67.22	1.609e-21	lte037.0-5.0-0.5a+0.2.BT-Settl.spec.7.dat
sdM1.5	LF	3500	5.0	−0.5	93.49	3.502e-22	lte035.0-5.0-0.5a+0.2.BT-Settl.spec.7.dat
sdM2.0	LF	3500	4.5	−1.5	60.84	1.051e-21	lte035.0-4.5-1.5a+0.4.BT-Settl.spec.7.dat
sdM2.5	LF	3600	5.0	−1.0	37.11	7.791e-22	lte036.0-5.0-1.0a+0.4.BT-Settl.spec.7.dat
sdM3.0	LF	3500	5.0	−0.0	88.51	2.208e-21	lte035.0-5.0-0.0a+0.0.BT-Settl.spec.7.dat
sdM3.5	LF	3400	5.0	−1.0	169.9	3.924e-21	lte034.0-5.0-1.0a+0.4.BT-Settl.spec.7.dat
sdM4.0	LF	3400	5.0	−1.0	58.22	1.54e-21	lte034.0-5.0-1.0a+0.4.BT-Settl.spec.7.dat
sdM4.5	LF	3300	5.0	−1.5	66.55	2.115e-22	lte033.0-5.0-1.5a+0.4.BT-Settl.spec.7.dat
sdM5.0	LF	3100	5.5	−0.5	98.69	6.395e-22	lte031.0-5.5-0.5a+0.2.BT-Settl.spec.7.dat
sdM5.5	LF	3100	5.0	−1.5	66.45	3.139e-22	lte031.0-5.0-1.5a+0.4.BT-Settl.spec.7.dat
sdM6.0	LF	3100	4.5	−1.5	66.98	3.779e-22	lte031.0-4.5-1.5a+0.4.BT-Settl.spec.7.dat
sdM6.5	LF	2800	4.5	−2.5	8854	5.129e-21	lte028.0-4.5-2.5a+0.4.BT-Settl.spec.7.dat
sdM8.0	LF	3000	5.0	−2.5	83.22	2.962e-22	lte030.0-5.0-2.5a+0.4.BT-Settl.spec.7.dat
sdM9.5	LF	3000	5.0	−2.5	63.45	8.95e-22	lte030.0-5.0-2.5a+0.4.BT-Settl.spec.7.dat
esdM0.0	LF	3800	5.0	−1.0	46.36	1.789e-22	lte038.0-5.0-1.0a+0.4.BT-Settl.spec.7.dat
esdM0.5	LF	3700	5.0	−2.0	29.55	4.919e-22	lte037.0-5.0-2.0a+0.4.BT-Settl.spec.7.dat
esdM1.0	LF	3600	4.5	−2.0	72.12	2.124e-22	lte036.0-4.5-2.0a+0.4.BT-Settl.spec.7.dat
esdM1.5	LF	3500	4.5	−2.0	29.95	7.937e-22	lte035.0-4.5-2.0a+0.4.BT-Settl.spec.7.dat
esdM2.0	LF	3500	4.5	−2.0	91.63	2.571e-22	lte035.0-4.5-2.0a+0.4.BT-Settl.spec.7.dat
esdM3.0	LF	3500	5.0	−1.5	97.21	6.376e-22	lte035.0-5.0-1.5a+0.4.BT-Settl.spec.7.dat
esdM3.5	LF	3400	5.0	−2.0	44.81	2.134e-22	lte034.0-5.0-2.0a+0.4.BT-Settl.spec.7.dat
esdM4.0	LF	3400	5.0	−1.5	55	2.057e-22	lte034.0-5.0-1.5a+0.4.BT-Settl.spec.7.dat
esdM4.5	LF	3200	4.5	−2.0	439	4.69e-21	lte032.0-4.5-2.0a+0.4.BT-Settl.spec.7.dat
esdM5.0	LF	3200	4.5	−2.0	43.03	1.99e-22	lte032.0-4.5-2.0a+0.4.BT-Settl.spec.7.dat
esdM5.5	LF	3200	5.0	−2.0	92.35	1.738e-21	lte032.0-5.0-2.0a+0.4.BT-Settl.spec.7.dat
esdM6.0	LF	3200	4.5	−2.0	30.38	9.303e-23	lte032.0-4.5-2.0a+0.4.BT-Settl.spec.7.dat
esdM6.5	LF	3200	5.0	−2.0	88.16	2.966e-22	lte032.0-5.0-2.0a+0.4.BT-Settl.spec.7.dat
esdM7.0	LF	3000	4.5	−2.0	10.14	1.032e-22	lte030.0-4.5-2.0a+0.4.BT-Settl.spec.7.dat
esdM7.5	LF	3000	5.0	−2.0	75.73	8.239e-22	lte030.0-5.0-2.0a+0.4.BT-Settl.spec.7.dat
esdM8.5	LF	3000	5.0	−2.5	50.75	4.173e-22	lte030.0-5.0-2.5a+0.4.BT-Settl.spec.7.dat
usdM0.0	LF	3600	5.5	−2.5	232.8	2.315e-22	lte036.0-5.5-2.5a+0.4.BT-Settl.spec.7.dat
usdM0.5	LF	3800	5.5	−2.0	36.52	7.582e-23	lte038.0-5.5-2.0a+0.4.BT-Settl.spec.7.dat
usdM1.0	LF	3600	5.0	−2.0	39.32	1.403e-22	lte036.0-5.0-2.0a+0.4.BT-Settl.spec.7.dat
usdM2.5	LF	3500	5.0	−2.0	45.49	1.938e-22	lte035.0-5.0-2.0a+0.4.BT-Settl.spec.7.dat
usdM3.0	LF	3600	5.5	−2.0	43.27	1.199e-22	lte036.0-5.5-2.0a+0.4.BT-Settl.spec.7.dat
usdM4.0	LF	3300	5.0	−2.0	10.1	2.222e-22	lte033.0-5.0-2.0a+0.4.BT-Settl.spec.7.dat
usdM4.5	LF	3400	5.0	−2.0	103	2.461e-22	lte034.0-5.0-2.0a+0.4.BT-Settl.spec.7.dat
usdM5.0	LF	3500	5.5	−2.0	206.1	5.591e-22	lte035.0-5.5-2.0a+0.4.BT-Settl.spec.7.dat
usdM5.5	LF	3400	5.5	−2.0	13.36	4.883e-23	lte034.0-5.5-2.0a+0.4.BT-Settl.spec.7.dat
usdM6.0	LF	3300	5.0	−2.0	49.56	4.229e-22	lte033.0-5.0-2.0a+0.4.BT-Settl.spec.7.dat
usdM7.5	LF	3100	5.0	−2.0	62.7	3.727e-22	lte031.0-5.0-2.0a+0.4.BT-Settl.spec.7.dat
usdM8.5	LF	3100	5.5	−2.5	49.69	4.503e-22	lte031.0-5.5-2.5a+0.4.BT-Settl.spec.7.dat

Notes. For each spectral subtype and metal class, we list the best fits with effective temperature (T_{eff}), gravity (log g), metallicity (M/H), chi^2 value, factor, and the name of the model.

Table B.5. Derived physical parameters for sdMs, esdMs, and usdMs from the comparison between the optical region (600–1000 nm; "VV") of the observed X-shooter spectra and the BT-Settl synthetic spectra.

SpT	Range	$T_{\rm eff}$	log g	M/H	chi^2	Factor	Model
sdM0.0	VV	3500	4.5	−2.5	1.506	2.581e-22	lte035.0-4.5-2.5a+0.4.BT-Settl.spec.7.dat
sdM0.5	VV	3700	4.5	−1.0	72.9	1.816e-21	lte037.0-4.5-1.0a+0.4.BT-Settl.spec.7.dat
sdM1.0	VV	3700	5.0	−0.5	66.12	1.636e-21	lte037.0-5.0-0.5a+0.2.BT-Settl.spec.7.dat
sdM1.5	VV	3400	4.5	−1.5	48.5	3.784e-22	lte034.0-4.5-1.5a+0.4.BT-Settl.spec.7.dat
sdM2.0	VV	3500	4.5	−1.0	48.26	1.082e-21	lte035.0-4.5-1.0a+0.4.BT-Settl.spec.7.dat
sdM2.5	VV	3500	4.5	−1.0	35.1	9.046e-22	lte035.0-4.5-1.0a+0.4.BT-Settl.spec.7.dat
sdM3.0	VV	3500	5.0	−0.0	89.26	2.224e-21	lte035.0-5.0-0.0a+0.0.BT-Settl.spec.7.dat
sdM3.5	VV	3400	5.0	−0.5	153.6	4.033e-21	lte034.0-5.0-0.5a+0.2.BT-Settl.spec.7.dat
sdM4.0	VV	3400	5.5	−0.5	47.24	1.627e-21	lte034.0-5.5-0.5a+0.2.BT-Settl.spec.7.dat
sdM4.5	VV	3100	4.5	−1.5	64.16	2.845e-22	lte031.0-4.5-1.5a+0.4.BT-Settl.spec.7.dat
sdM5.0	VV	3200	5.5	−0.0	57.52	5.62e-22	lte032.0-5.5-0.0a+0.0.BT-Settl.spec.7.dat
sdM5.5	VV	3200	5.5	−1.0	69.85	2.79e-22	lte032.0-5.5-1.0a+0.4.BT-Settl.spec.7.dat
sdM6.0	VV	3000	4.5	−1.5	60.23	4.532e-22	lte030.0-4.5-1.5a+0.4.BT-Settl.spec.7.dat
sdM6.5	VV	2900	5.5	−0.0	367.4	4.09e-21	lte029.0-5.5-0.0a+0.0.BT-Settl.spec.7.dat
sdM8.0	VV	2800	5.0	−2.5	55.29	3.348e-22	lte028.0-5.0-2.5a+0.4.BT-Settl.spec.7.dat
sdM9.5	VV	2600	4.5	−2.5	28.39	1.454e-21	lte026.0-4.5-2.5a+0.4.BT-Settl.spec.7.dat
esdM0.0	VV	3600	4.5	−1.5	51.33	2.339e-22	lte036.0-4.5-1.5a+0.4.BT-Settl.spec.7.dat
esdM0.5	VV	3600	4.5	−1.5	33.95	5.464e-22	lte036.0-4.5-1.5a+0.4.BT-Settl.spec.7.dat
esdM1.0	VV	3600	4.5	−1.5	54.39	2.181e-22	lte036.0-4.5-1.5a+0.4.BT-Settl.spec.7.dat
esdM1.5	VV	3400	4.5	−1.5	31.73	9.081e-22	lte034.0-4.5-1.5a+0.4.BT-Settl.spec.7.dat
esdM2.0	VV	3400	4.5	−1.5	65.67	2.973e-22	lte034.0-4.5-1.5a+0.4.BT-Settl.spec.7.dat
esdM3.0	VV	3400	5.0	−1.5	81.18	7.466e-22	lte034.0-5.0-1.5a+0.4.BT-Settl.spec.7.dat
esdM3.5	VV	3400	5.0	−1.5	43.41	2.206e-22	lte034.0-5.0-1.5a+0.4.BT-Settl.spec.7.dat
esdM4.0	VV	3200	4.5	−2.0	61.63	2.746e-22	lte032.0-4.5-2.0a+0.4.BT-Settl.spec.7.dat
esdM4.5	VV	3200	4.5	−1.5	326.9	4.852e-21	lte032.0-4.5-1.5a+0.4.BT-Settl.spec.7.dat
esdM5.0	VV	3200	4.5	−1.5	45.1	1.963e-22	lte032.0-4.5-1.5a+0.4.BT-Settl.spec.7.dat
esdM5.5	VV	3100	4.5	−2.0	88.56	2.14e-21	lte031.0-4.5-2.0a+0.4.BT-Settl.spec.7.dat
esdM6.0	VV	3200	5.0	−2.0	29.11	9.46e-23	lte032.0-5.0-2.0a+0.4.BT-Settl.spec.7.dat
esdM6.5	VV	3100	4.5	−2.0	86.41	3.646e-22	lte031.0-4.5-2.0a+0.4.BT-Settl.spec.7.dat
esdM7.0	VV	3000	4.5	−2.0	5.132	9.173e-23	lte030.0-4.5-2.0a+0.4.BT-Settl.spec.7.dat
esdM7.5	VV	3000	5.0	−2.0	89.47	8.325e-22	lte030.0-5.0-2.0a+0.4.BT-Settl.spec.7.dat
esdM8.5	VV	2800	4.5	−2.5	52.36	5.534e-22	lte028.0-4.5-2.5a+0.4.BT-Settl.spec.7.dat
usdM0.0	VV	3500	4.5	−2.5	51.01	2.583e-22	lte035.0-4.5-2.5a+0.4.BT-Settl.spec.7.dat
usdM0.5	VV	3600	5.0	−2.5	42.57	9.734e-23	lte036.0-5.0-2.5a+0.4.BT-Settl.spec.7.dat
usdM1.0	VV	3600	5.0	−1.5	40.24	1.445e-22	lte036.0-5.0-1.5a+0.4.BT-Settl.spec.7.dat
usdM2.5	VV	3400	4.5	−2.0	50.77	2.315e-22	lte034.0-4.5-2.0a+0.4.BT-Settl.spec.7.dat
usdM3.0	VV	3400	4.5	−2.0	40.27	1.684e-22	lte034.0-4.5-2.0a+0.4.BT-Settl.spec.7.dat
usdM4.0	VV	3500	5.5	−2.0	2.578	1.425e-22	lte035.0-5.5-2.0a+0.4.BT-Settl.spec.7.dat
usdM4.5	VV	3300	5.0	−2.0	83.97	2.923e-22	lte033.0-5.0-2.0a+0.4.BT-Settl.spec.7.dat
usdM5.0	VV	3400	5.5	−2.5	131.2	6.592e-22	lte034.0-5.5-2.5a+0.4.BT-Settl.spec.7.dat
usdM5.5	VV	3800	6.0	−0.5	16.71	2.727e-23	lte038.0-6.0-0.5a+0.2.BT-Settl.spec.7.dat
usdM6.0	VV	3200	5.0	−2.0	44.45	4.976e-22	lte032.0-5.0-2.0a+0.4.BT-Settl.spec.7.dat
usdM7.5	VV	3000	5.0	−2.5	28.43	4.579e-22	lte030.0-5.0-2.5a+0.4.BT-Settl.spec.7.dat
usdM8.5	VV	3000	5.5	−2.5	51.61	5.169e-22	lte030.0-5.5-2.5a+0.4.BT-Settl.spec.7.dat

Notes. For each spectral subtype and metal class, we list the best fits with effective temperature ($T_{\rm eff}$), gravity (log g), metallicity (M/H), chi^2 value, factor, and the name of the model.